Evaluation of ice hydrometeor retrieval using multi-band radar and millimeter-wave radiometer measurements from the IMPACTS campaign

Keiichi Ohara[1,2], Hirohiko Masunaga[3]

[1] Earth Observation Research Center, Japan Aerospace Exploration Agency, Ibaraki, Japan
[2] Graduate School of Environmental Studies, Nagoya University, Nagoya, Japan
[3] Institute for Space-Earth Environmental Research, Nagoya University, Nagoya, Japan

Correspondence to: Keiichi Ohara（ohara.keiichi@jaxa.jp)

Abstract.

Understanding the microphysical properties of ice hydrometeors remains challenging. This study develops and evaluates a cloud-ice retrieval algorithm that synergistically uses W-band radar, Ku/Ka-band radar, and millimeter-wave radiometer observations. This strategy enables to observe deep inside precipitating clouds unreachable by conventional combined radar–lidar measurements due to severe attenuation.

The retrieved cloud microphysical parameters are compared with aircraft in situ measurements from the Investigation of Microphysics and Precipitation for Atlantic Coast-Threatening Snowstorms (IMPACTS) campaign. The bias between retrieved values and in situ measurements varied by roughly two orders of magnitude depending on the particle habit assumptions. A mixture of rosette and snowflake habits based on physical considerations yielded the best overall performance. Under this habit assumption, the mean ratios of the retrieved values to in situ probe measurements of ice water content (IWC), total number concentration (N_t), mass-weighted mean diameter (D_m) are 1.01, 0.97, and 1.05. The mean bias and RMSE for terminal fall velocity (V_t) are −0.02 m s^{-1} and 0.30 m s^{-1}. Forward-simulated measurements from the retrieved profiles reproduce the actual radars and radiometer observations well, confirming the self-consistency of the current algorithm.

A theoretical sensitivity analysis demonstrates that the radar–radiometer synergy becomes particularly effective in deep cloud layers where particle sizes are large, ensuring that the multi-sensor retrieval outperform the W-band radar-only retrieval especially deep inside clouds. These results highlight the potential of combining multi-band radar and millimeter-wave radiometer observations to advance our understanding of ice-hydrometeor microphysics in deep precipitating clouds.

1 Introduction

In developed precipitation systems, ice hydrometeors such as cloud ice, snowflakes, and graupel play crucial roles in cloud microphysical processes and precipitation formation. In convective clouds, intense updrafts promote riming and coalescence, leading to the formation of ~~graupel~~graupels and ~~hail~~hails that cause locally intense precipitation. In contrast, within stratiform clouds, relatively weak updrafts allow ice crystals and snowflakes to gradually grow through vapor deposition and aggregation as they slowly fall toward the surface, producing widespread and weak precipitation. These microphysical processes are well documented in the literature as a key feature of organized precipitation systems (Houze, 2014). However, global-scale observations to verify the ice cloud microphysics remain limited.

One of the remaining challenges is technical difficulties in estimating the microphysical properties of ice hydrometeors from observations. Conventional satellite remote sensing by use of any single instrument alone often fails to simultaneously constrain various cloud-microphysical parameters such as particle size distribution and particle shape. A promising strategy to overcome this limitation is combining multiple sensors with different wavelengths and measurement principles. Notable examples include combined observations from the CloudSat and Cloud–Aerosol Lidar and Infrared Pathfinder Satellite Observations (CALIPSO) satellites, which carried a W-band radar and a lidar, respectively (Delanoë, J., and R. J. Hogan, 2008, 2010; Deng et al., 2015; Deng, M., G. G. Mace, Z. Wang, and H. Okamoto, 2010; Okamoto, 2003; Okamoto et al., 2010). This approach has been further adopted for the W-band radar–lidar synergy algorithm onboard the Earth Cloud, Aerosol and Radiation Explorer (EarthCARE) satellite (Illingworth et al., 2015; Sato et al., 2025; Wehr et al., 2023). However, lidar observations are strongly affected by in-cloud attenuation at the expense of an excellent detectability of optically thin clouds, making them unsuitable for retrieving ice hydrometeors within optically thick, precipitating clouds.

As an illustrative example, Fig. 1a shows the W-band radar reflectivity (Z_w) from Cloud Profiling Radar (CPR) aboard CloudSat as a color map and the cloud detection areas from Cloud-Aerosol LIdar with Orthogonal Polarization Lidar (CALIOP) aboard CALIPSO in gray shade. It is evident that lidar sensitivity is limited to near the cloud top due to strong attenuation, providing little information from deeper cloud layers. This means that the combined spaceborne radar–lidar observations do not provide a synergistic benefit for deep inside a thick cloud layer. Previous studies have also reported that retrieval uncertainties are particularly large in radar-only regions (Cazenave et al., 2019; Delanoë, J., and R. J. Hogan, 2008). In heavily precipitating clouds rich in snow and graupel, even W-band radar reflectivity suffers from strong attenuation, making it even more difficult to retrieve ice hydrometeors in the deeper cloud layers (Mason et al., 2023).

In Ohara and Masunaga (2025, hereafter O25), an ice-hydrometeor retrieval algorithm was developed to address this issue by combining spaceborne W-band radar and high-frequency microwave radiometer measurements. Among the goals of the present study is to extend this algorithm to incorporate Ku- and Ka-band radar observations as well. Figure 1b-c show the sensitivity of 165.5 GHz brightness temperature to IWC ($\left|\frac{\partial T_b}{\partial \log(IWC)}\right| > 1$K) from the Global Precipitation Measurement (GPM) Microwave Imager (GMI), and the Ku-band radar reflectivity observations ($Z_{Ku} > 15$ dBZ) from the Dual-frequency Precipitation Radar (DPR), together with the sensitivity domains of lidar (gray shading) and W-band radar (light-purple shading). These sensors are sensitive to ice hydrometeors in the deep layers of clouds, where lidar observations have no sensitivity. Therefore, combining observations from high-frequency microwave radiometers and Ku- and Ka-band radars with W-band radar measurements is expected to reduce retrieval uncertainties of ice-hydrometeor microphysical properties in the deep precipitating clouds.

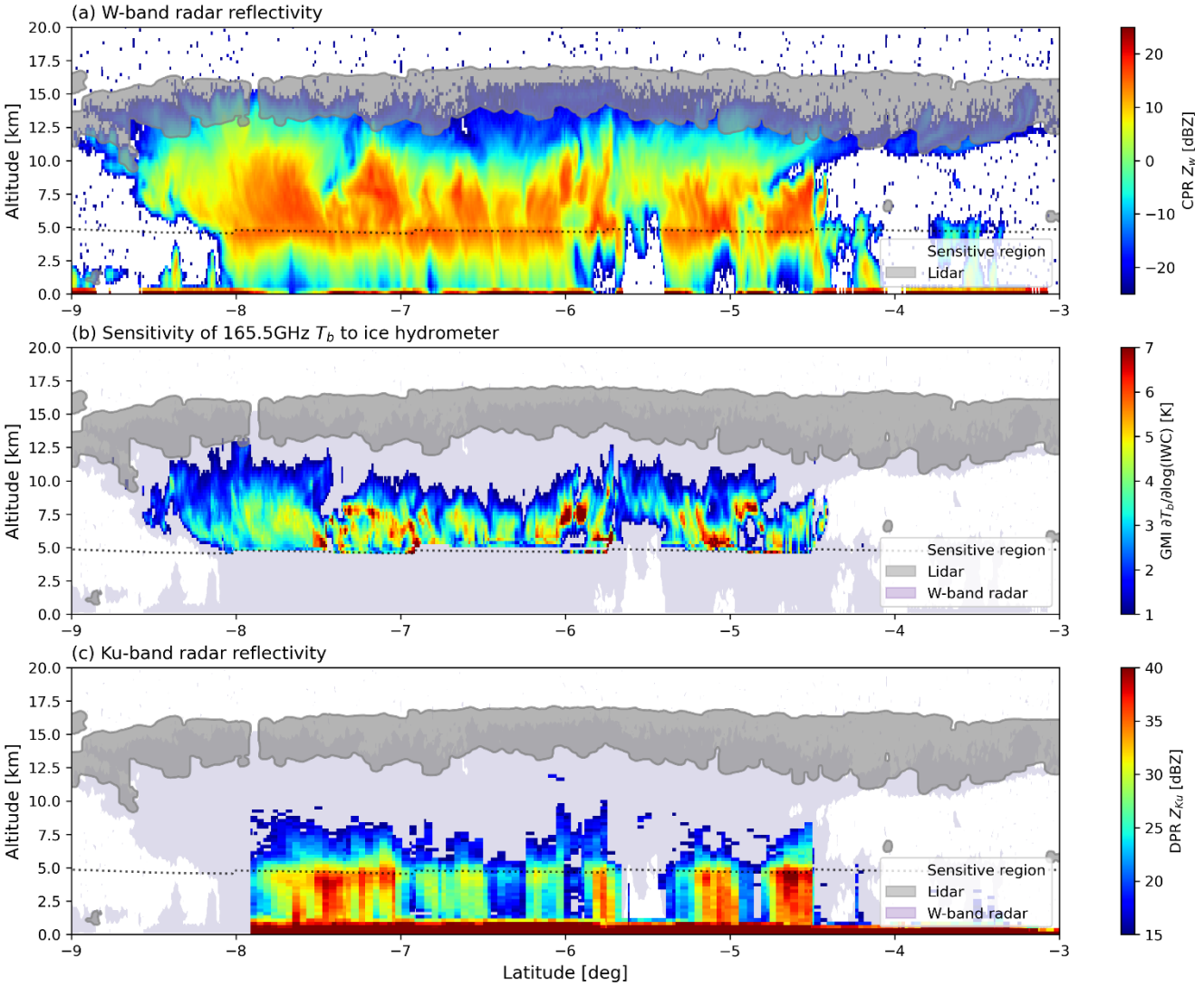

Figure 1: Sensitivities of various satellite-borne sensors to ice hydrometeors. (a) The color contours represent CloudSat/CPR W-band radar reflectivity. The gray shading indicates cloud detected regions where the cloud fraction observed by the CALIPSO lidar (CALIOP) exceeds 25%. (b) The sensitivity of the GPM/GMI brightness temperature at 166 GHz to perturbations of Ice Water Content ($\left|\frac{\partial T_b}{\partial log(IWC)}\right|$) in each layer. This value calculated from retrieved IWC in O25 using radiative transfer model. (c) The GPM Ku-band radar reflectivity. The black dashed line represents the 0 °C altitude.

The combined retrieval algorithm of O25 uses a matchup dataset between the CloudSat and GPM observations, while validation has yet to be performed in comparison with in situ observations. The objective of this study is to evaluate the performance of the O25 retrieval algorithm by applying it to airborne remote-sensing instruments and examining their results against in situ measurements obtained during the Investigation of Microphysics and Precipitation for Atlantic Coast-

Threatening Snowstorms (IMPACTS) field campaign (McMurdie et al., 2022). Section 2 describes the IMPACTS datasets, the forward model, and the ~~atmospheric reanalysis~~ancillary data used in the retrieval algorithm. Section 3 presents an overview of the retrieval methodology including cloud microphysical assumptions along with updates to the O25 algorithm. Section 4 evaluates the retrieval performance and examines the influence of particle habit assumptions on the retrieval accuracy. Section 5 assesses the particle fall velocity diagnosed from the retrieved microphysical parameters using in situ probe measurements and W-band Doppler radar observations. It also discusses the improvement in retrieval accuracy through the synergistic use of multiple microwave sensors. Finally, Section 6 summarizes the overall findings of this study.

2 Data and Preprocessing

2.1 IMPACTS dataset

The IMPACTS field campaign, conducted during the winters of 2020, 2022, and 2023, was a comprehensive observational program designed to investigate the microphysical and dynamical processes of snowstorms along the eastern United States. Coordinated measurements were made using NASA's ER-2 high-altitude aircraft and the P-3 cloud-sampling aircraft. The ER-2 carried a set of remote-sensing instruments, including high-frequency microwave radiometers and W-, Ku-, and Ka-band Doppler radars, while the P-3 carried in situ microphysical probes and meteorological sensors for detailed measurements of cloud and precipitation particles. The integration of these datasets offers a valuable testbed for validating and improving a multi-sensor algorithm to retrieve ice hydrometeors.

Table 1 lists the IMPACTS flight cases analyzed in this study, including observation dates, scenes (ocean or land), the dominant cloud–precipitation type, and the number of microwave radiometer footprints. Only cases with coincident ER-2 and P-3 observations that have a temporal difference between the two platforms within 15 minutes are selected. A match-up is adopted when the P-3 flight track is located within the ER-2 microwave radiometer footprint and all the necessary parameters for algorithm input and validation are available. The cloud–precipitation types are classified using W-band echo-top temperature (< -20 °C for deep, ≥ -20 °C for shallow) (Aoki et al., 2025), presence or absence of strong updrafts in the W-band Doppler velocity (convective or stratiform), and near-surface air temperature (> 0 °C for rainfall, < 0 °C for snowfall).

Date	Scene (ocean or land)	Cloud and precipitation type	Number of microwave radiometer footprints
2020/01/25	Ocean	Deep convective rainfall	68

2020/01/25	Land	Deep stratiform rainfall	395
2020/02/01	Ocean	Shallow stratiform rainfall	117
2020/02/05	Land	Deep stratiform snowfall	437
2022/02/08	Ocean	Shallow stratiform rainfall	76
2022/02/08	Land	Shallow stratiform snowfall	58
2022/02/13	Land	Shallow stratiform snowfall	35
2022/02/17	Land	Deep stratiform snowfall	437

Table 1: IMPACTS flight cases that satisfy the ER-2 and P-3 match-up criteria.

2.1.1 Radar and radiometer observations from ER-2 aircraft

The ER-2 aircraft flies at an altitude of approximately 20 km carrying nadir-looking instruments as listed in Table 2. The Cloud Radar System (CRS) (Li et al., 2004) is a W-band radar that shares the same operating frequency as the CloudSat/CPR and EarthCARE/CPR and is equipped with Doppler capability. The Conical Scanning Millimeter-wave Imaging Radiometer (CoSMIR) (Wang et al., 2013) is equipped with high-frequency channels at 89, 165.5, and 183 ± 3, 7 GHz, which ~~are~~correspond to the ~~same frequencies as those used by the~~high-frequency channels (≥89 GHz) of GPM/GMI ~~instrument~~. The High Altitude Imaging Wind and Rain Airborne Profiler (HIWRAP) (Li et al., 2016) is a dual-frequency (Ku- and Ka-band) radar system that employs the same frequencies as the GPM/DPR. The similarity in microwave frequencies between the airborne and satellite sensors ensures that the framework of the multi-sensor retrieval algorithm developed by O25 using coincident CloudSat–GPM observations can be applied to the ER-2 measurements as well. CoSMIR brightness temperatures (T_b) at 89, 165.5, and 183 ± 3, ±7 GHz (only same channels as GMI) are used. HIWRAP Ku- and Ka-band radar reflectivity (Z_{Ku} and Z_{Ka}) data above 15 dBZ (almost same as DPR sensitivity limit) are utilized, while Doppler velocities are not used. For CRS data, W-band radar reflectivity (Z_w) above –30 dBZ (almost same as CPR sensitivity limit) and Doppler velocity (V_d) are used.

Sensor name	Sensor type	Frequency [GHz]	Observations used for algorithm input	Horizontal resolution [m]	Vertical resolution [m]	Similar spaceborne sensor

CoSMIR	Microwave radiometer	50.3 H, 52.8 H, 89.0 V/H, 165.5 V/H, 183±1 H, ±3 H, ±7 H	Brightness temperatures (T_b) at nadir-viewing	1400 x 1400 (nadir)	N/A	GPM/GMI GOSAT-GW/AMSR3
CRS	W-band doppler radar	94.0	Radar reflectivity (Z_w ~~>~~ >-30dBZ), Doppler velocity (V_d)	160	115	CloudSat/CPR EarthCARE/CPR
HIWRAP	Ku-band doppler radar	13.91	Radar reflectivity (Z_{Ku}>15dBZ)	1050	145	GPM/DPR
	Ka-band doppler radar	35.56	Radar reflectivity (Z_{Ka}>15dBZ)	420	145	

Table 2: Specifications of sensors onboard ER-2 aircraft.

Figure 2a illustrates the footprint sizes and sampling intervals of the sensors—CoSMIR (nadir-viewing), CRS, and HIWRAP. The CoSMIR footprint is substantially larger than those of the radar instruments, and the difference in spatial resolution among the sensors can be a source of retrieval error in the multi-sensor algorithm. To mitigate this effect, CRS and HIWRAP observations located within each CoSMIR footprint ~~are~~ averaged using a Gaussian weight representing the ~~GoSMIR~~CoSMIR antenna pattern before input to the algorithm. The averaging of radar reflectivity is performed in linear units ([mm^6 m^{-3}]). Figure 2b shows the aircraft flight tracks and the column-integrated water vapor for an over-ocean case on 25 January 2025. Figure 2c presents the CoSMIR high-frequency T_b for this case, while Figs. 2d-g show the footprint-adjusted CRS Z_w, V_d, and the HIWRAP Z_{Ku}, Z_{Ka} vertical profiles. The black dashed line indicates the 0 °C level, where a distinct bright band is evident particularly in Z_{Ku} and Z_{Ka}, accompanied by a pronounced increase in negative V_d. These are as expected to occur as the result of the melting of solid precipitation particles into raindrops.

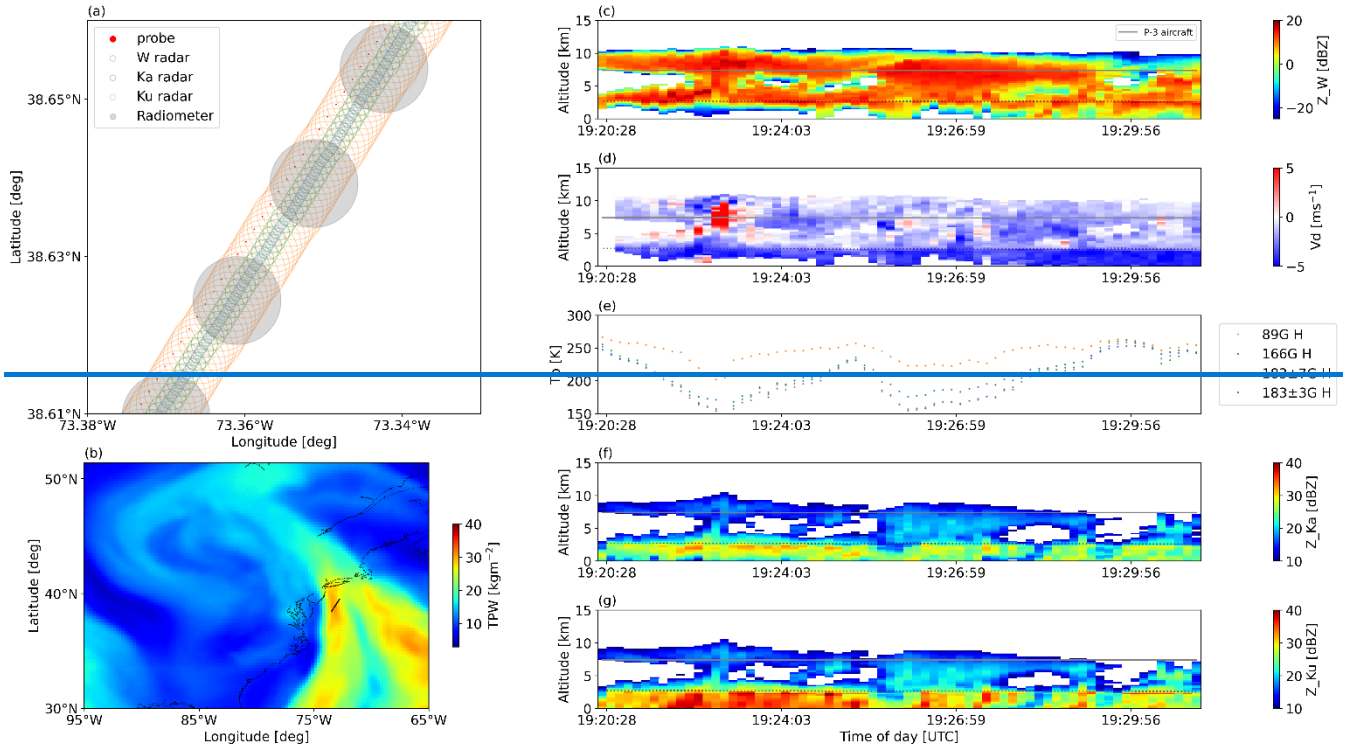
(a)
probe
W radar
Ka radar
Ku radar
Radiometer
38.65°N
38.63°N
38.61°N
Latitude [deg]
73.38°W
73.36°W
73.34°W
Longitude [deg]
(b)
50°N
40°N
30°N
Latitude [deg]
95°W
85°W
75°W
65°W
Longitude [deg]
TPW [kgm^{-2}]
40
30
20
10
(c)
P-3 aircraft
Altitude [km]
Z_W [dBZ]
(d)
Vd [ms^{-1}]
(e)
Tb [K]
89G H
166G H
183±3G H
(f)
Z_Ka [dBZ]
(g)
Z_Ku [dBZ]
19:20:28
19:24:03
19:26:59
19:29:56
Time of day [UTC]

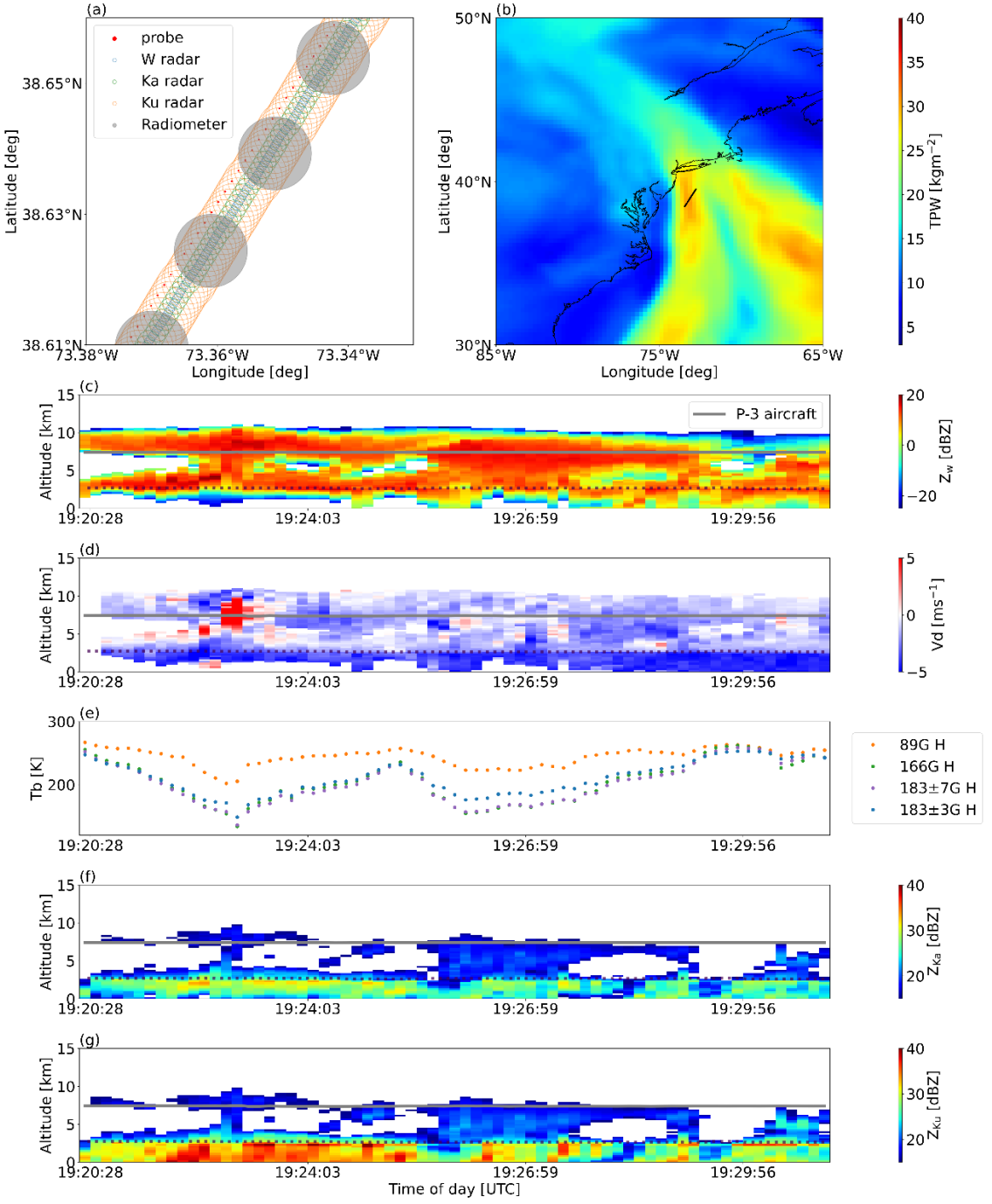

Figure 2: An example of observations by multiple sensors aboard the ER-2 aircraft on 25 January 2025. (a) Comparison of footprint sizes and sampling intervals among the ER-2-borne CoSMIR (radiometer), CRS (W-band radar), HIWRAP (Ku- and Ka-band radar), and the in-situ probes onboard the P-3 aircraft. (b) Flight track (black line) and the surrounding distribution of column-integrated water vapor (color map). (c) CoSMIR (nadir) brightness temperatures at 89, 165.5, and 183 ± 3/7 GHz. (d) CRS W-band

radar reflectivity. (e) CRS Doppler velocity. (f) HIWRAP ~~Ku~~Ka-band radar reflectivity. (g) HIWRAP ~~Ka~~Ku-band radar reflectivity. The gray solid line indicates the P-3 flight altitude, and the black dashed line indicates the 0 °C level.

2.1.2 In situ observations from P-3 aircraft

Table 3 lists the in situ instruments onboard the P-3 aircraft and the physical quantities used for algorithm validation. The Two-Dimensional Stereo probe (2D-S) and the High-Volume Precipitation Spectrometer (HVPS-3) are optical array probes that record two-dimensional shadow images of particles passing through horizontal and vertical arrays to measure particle size distributions (PSD) and area ratios A_r (the ratio of particle cross-sectional area to the area of the circumscribed circle) (Field et al., 2006; Lawson et al., 2006). In this study, the mean of the horizontal and vertical array measurements is used when they are both valid. When one array data is missing, the valid one is adopted. The 2D-S is suitable for detecting particles smaller than approximately 1 mm, while the HVPS-3 is optimized for larger particles exceeding 1 mm. A merged product combining 2D-S and HVPS-3 observations is used to obtain PSD and A_r data. The P-3 aircraft also records the observation time, position (latitude and longitude), flight altitude, temperature, humidity, and pressure. These data were obtained from the P-3 Meteorological and Navigation Data products.

The sampling intervals of the probe measurements are shown as red dots in Fig 2a. As done for the radar observations, the probe measurements are spatially averaged within each CoSMIR footprint using Gaussian. The P-3 flight altitude during the case shown in Fig. 2 is indicated by gray solid lines in Figs. 2d-g. The examples of PSD and A_r measurements at this altitude are shown in Figs. 3a-b. From these microphysical probe measurements, several parameters used for algorithm validation are derived, including ice water content (IWC), total number concentration (N_t), mass-weighted mean diameter (D_m), and Z_w-weighted terminal fall velocity (V_t).

Sensor or data name	Measurements	Physical quantities used for evaluation
2D-S probe	Distribution of particle size and Area ratio for the size range from 100 um to 1mm	Ice water content (IWC), number of concentration (N_t), mass-weighted diameter (D_m) and Z_w -weighted terminal fall velocity (V_t)
HVPS-3 probe	Distribution of particle size and Area ratio for the size range from 1 mm to 3mm	
P-3 Meteorological and Navigation Data	Observation time, latitude, longitude, altitude, temperature, humidity and pressure	Temperature, humidity and pressure data are used for calculation of V_t.

Table 3: P-3 aircraft in situ measurements used for algorithm evaluation.

The method used to derive the cloud microphysical parameters (IWC, N_t, D_m and V_t) from the probe observations of PSD and A_r is described below. The parameters N_t, D_m and IWC are obtained from the measured PSD $N(D)$ using Eq. (1), (2) and (3):

$$N_t = \int_{100}^{\infty} N(D)dD \ , \tag{1}$$

$$D_m = \frac{\int_{100}^{\infty} D^4 N(D)dD}{\int_{100}^{\infty} D^3 N(D)dD} \tag{2}$$

$$IWC = \int_{100}^{\infty} m(D)N(D)dD \ , \tag{3}$$

Here, D represents the maximum dimension of a particle. The integral is applied to diameters larger than 100 μm only, because probe measurements for particles smaller than 100 μm are known to have large uncertainties. The mass–dimension relationship *m(D)* in Eq. (3) depends on the assumed particle habit. For consistency between the retrieval and validation, the same *m(D)* relationship as assumed in the combined retrieval algorithm is adopted in Eq. (3). Details of the *m(D)* relationship are described in Section 3.2. Fig. 3c shows examples of N_t derived from the PSD measurements in Fig. 3a using the above procedure.

The terminal fall velocity of individual particles, $v_t(D)$, is calculated from the PSD and A_r probe observations using the theoretical and empirical formulations proposed by (Heymsfield and Westbrook, 2010) as expressed by Eqs. (4)-(6):

$$X^*(D) = \frac{\rho_{air}\, 8m(D)g}{\eta^2\, \pi (A_r(D))^{\frac{1}{2}}} \tag{4}$$

$$Re(D) = \frac{\delta_0^2}{4}\left[\left(1 + \frac{4\sqrt{X^*(D)}}{\delta_0^2\sqrt{C_0}}\right)^{\frac{1}{2}} - 1\right]^2 \tag{5}$$

$$v_t(D) = \frac{\eta Re(D)}{\rho_{air} D} \tag{6}$$

Here, ρ_{air} is the air density, η is the dynamic viscosity, both calculated using the temperature and pressure data from the P-3 Meteorological and Navigation Data. g denotes the gravitational acceleration. The boundary-layer depth δ_0 and pressure drag coefficient C_0 are taken from the coefficients used by Heymsfield and Westbrook (2010). X^* represents the Best number, and Re denotes the Reynolds number. For validation using W-band Doppler velocity observations, it is convenient to use the terminal fall velocity weighted by the PSD and W-band backscattering cross section $\sigma_b(D)$ defined as

$$V_t = \frac{\int_{100}^{\infty} v_t(D)N(D)\sigma_b(D)dD}{\int_{100}^{\infty} N(D)\sigma_b(D)dD} \tag{7}$$

Because $\sigma_b(D)$ depends on the assumed particle habit, the same $\sigma_b(D)$ as used in the combined retrieval algorithm (Section 3.2) is employed. Fig. 3d shows the Z_w-weighted terminal fall velocity V_t calculated from the PSD and A_r measurements in Figs. 3a-b.

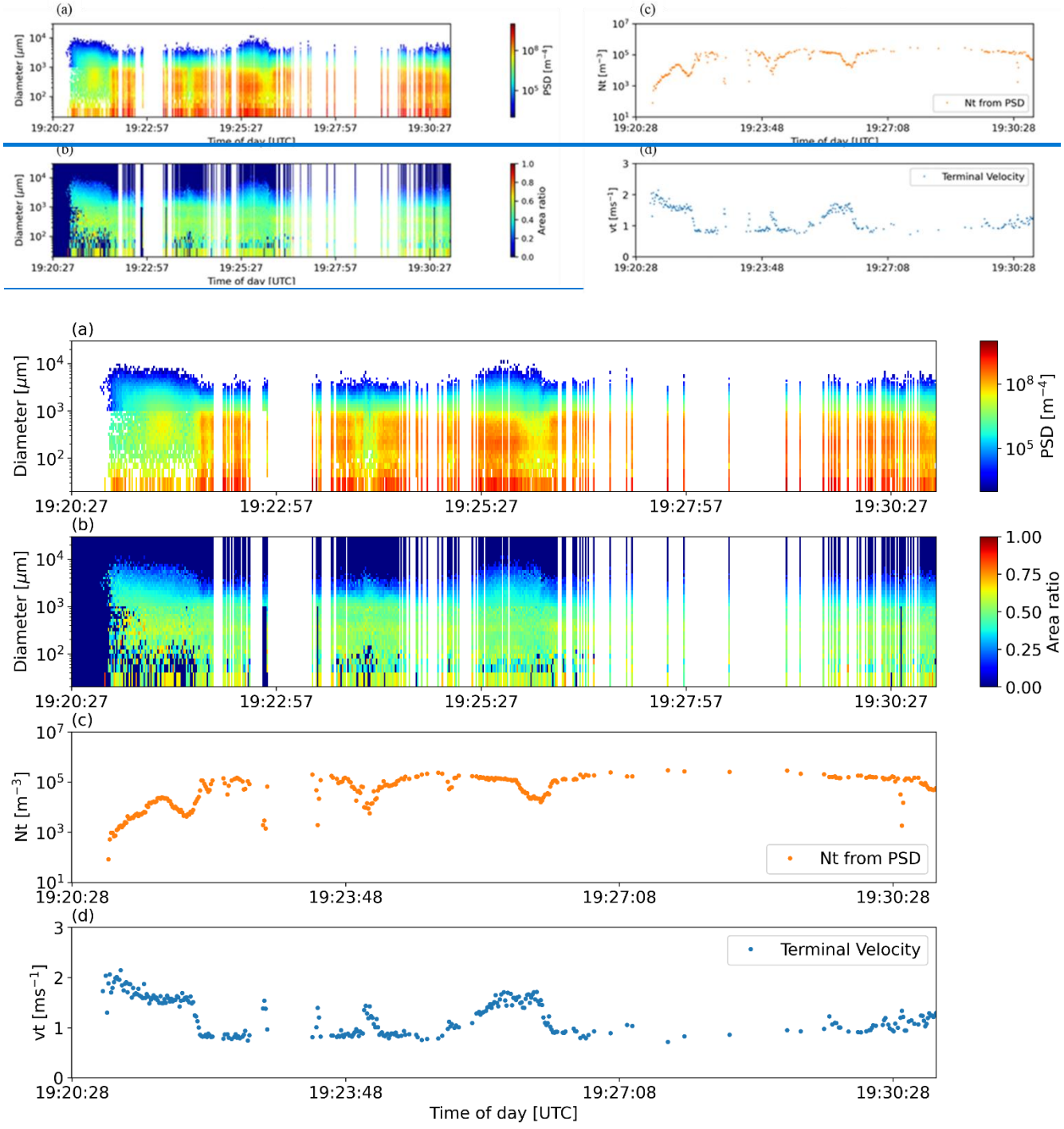
(a)
Diameter [μm]
PSD [m⁻⁴]
(b)
Diameter [μm]
Area ratio
(c)
Nt [m⁻³]
Nt from PSD
(d)
vt [ms⁻¹]
Terminal Velocity
19:20:27
19:22:57
19:25:27
19:27:57
19:30:27
19:20:28
19:23:48
19:27:08
19:30:28
Time of day [UTC]

195

Figure 3: Example of in situ probe measurements from the P-3 aircraft. (a) Particle size distribution (PSD). (b) Area ratio (A_r) distribution. (c) Total number concentration (N_t) and (d) Z_w-weighted terminal fall velocity (V_t) calculated from the PSD in (a) and A_r in (b).

2.2 Forward model and ancillary data

The combined retrieval algorithm for ice hydrometeors employs the Joint Simulator for Satellite Sensors (J-sim) developed by the Japan Aerospace Exploration Agency (JAXA) (Hashino et al., 2013, 2016) for forward simulations. J-sim contains the Satellite Data Simulator Unit (SDSU) (Masunaga et al., 2010), which enables simulation of a wide range of microwave satellite observations, including W-band Doppler radar, Ku- and Ka-band radar, and microwave radiometers (Ohara et al., 2023, 2025). J-sim is also applicable to analogous airborne sensors such as CRS, CoSMIR, and HIWRAP.

As ancillary data for the forward calculations, vertical profiles of temperature, water vapor, and pressure, as well as surface temperature and sea surface wind speed, are taken from the ERA5 hourly reanalysis data (Copernicus Climate Change Service, 2018). Within cloudy and precipitating regions (Zw > −30 dBZ), relative humidity is set to 100% instead of using ERA5 values. These variables are treated as fixed inputs in the retrieval algorithm described in the next section.

Land surface emissivity is modeled by the NESDIS microwave land emissivity model (Weng et al., 2001) implemented in the radiative transfer model in use (J-Sim). The emissivity is calculated assuming a vegetation fraction of 100%, soil moisture fraction of 50%, surface temperature from ERA5 hourly data, and zero snow depth in this study. These simplified assumptions may introduce errors in surface emissivity, particularly under conditions such as snow cover, which could affect primarily low-frequency brightness temperatures. However, the high-frequency channels (≥89 GHz) used in this study are more strongly influenced by water vapor absorption and cloud/precipitation scattering, and thus have reduced sensitivity to the surface, suggesting that the impact is relatively small.

The vertical profile of liquid water content (LWC) is estimated from the HIWRAP Ku-band radar reflectivity using the Z_{Ku}–LWC relationship (Masunaga, 2022) derived under the assumption of the Marshall and Palmer (1948) raindrop size distribution and the Rayleigh-scattering approximation. The liquid particle size distribution is assumed to follow the exponential form $N_l(D) = N_{0,l} \exp(-\lambda_l D)$ of Marshall and Palmer (1948), where $N_{0,l} = 8000$ [$\mathrm{m^{-3}mm^{-1}}$], and λ_l varies as a function of LWC. Under these assumptions and the Rayleigh approximation, $LWC = 3.4 \times 10^{-3}\, Z_{Ku}^{4/7}$ is obtained (see Chapter 10.2.1 of Masunaga, 2022). The uncertainty associated with this LWC estimate is discussed in the Supplement. In the present retrieval framework, liquid and ice particles are treated separately based on temperature from ERA5 hourly data, and thus mixed-phase conditions are not considered. The treatment of supercooled liquid water is a potentially critical limitation of the current approach and should be addressed in future work.

3 Retrieval algorithm

3.1 Overview of combined algorithm

The structure of the retrieval algorithm is illustrated in Fig. 4. The overall framework is based on O25. In the first step, the algorithm rapidly estimates an initial guess of ice-hydrometeor profiles reasonably close to the solution, using an existing training dataset. In the second step, these initial values are refined through an optimal estimation (OE) method that updates the solution so it is further consistent with the multi-sensor observations along with estimated retrieval uncertainties. Finally, the terminal fall velocity of cloud and precipitation particles and the vertical air motion are estimated using the retrieved cloud-ice parameters and the observed W-band Doppler velocity (V_d).

This section briefly revisits the algorithm framework described in O25 and highlights the improvements implemented in this study. The major updates include: (1) the incorporation of a mixed-habit representation of nonspherical ice particles (Section 3.2); (2) an improved initial estimation method (Section 3.3); (3) the extension of the OE framework to include Z_{Ku} and Z_{Ka} profiles in addition to Z_w profile and high-frequency T_b (Section 3.3); and (4) the estimation of terminal fall velocity and vertical air motion (Section 3.3). Finally, Section 3.4 presents theoretical sensitivity experiments to demonstrate the difference in scattering characteristics captured by high-frequency T_b, Z_w, Z_{Ku} and Z_{Ka} measurements, as well as the expected synergistic benefits among these sensors.

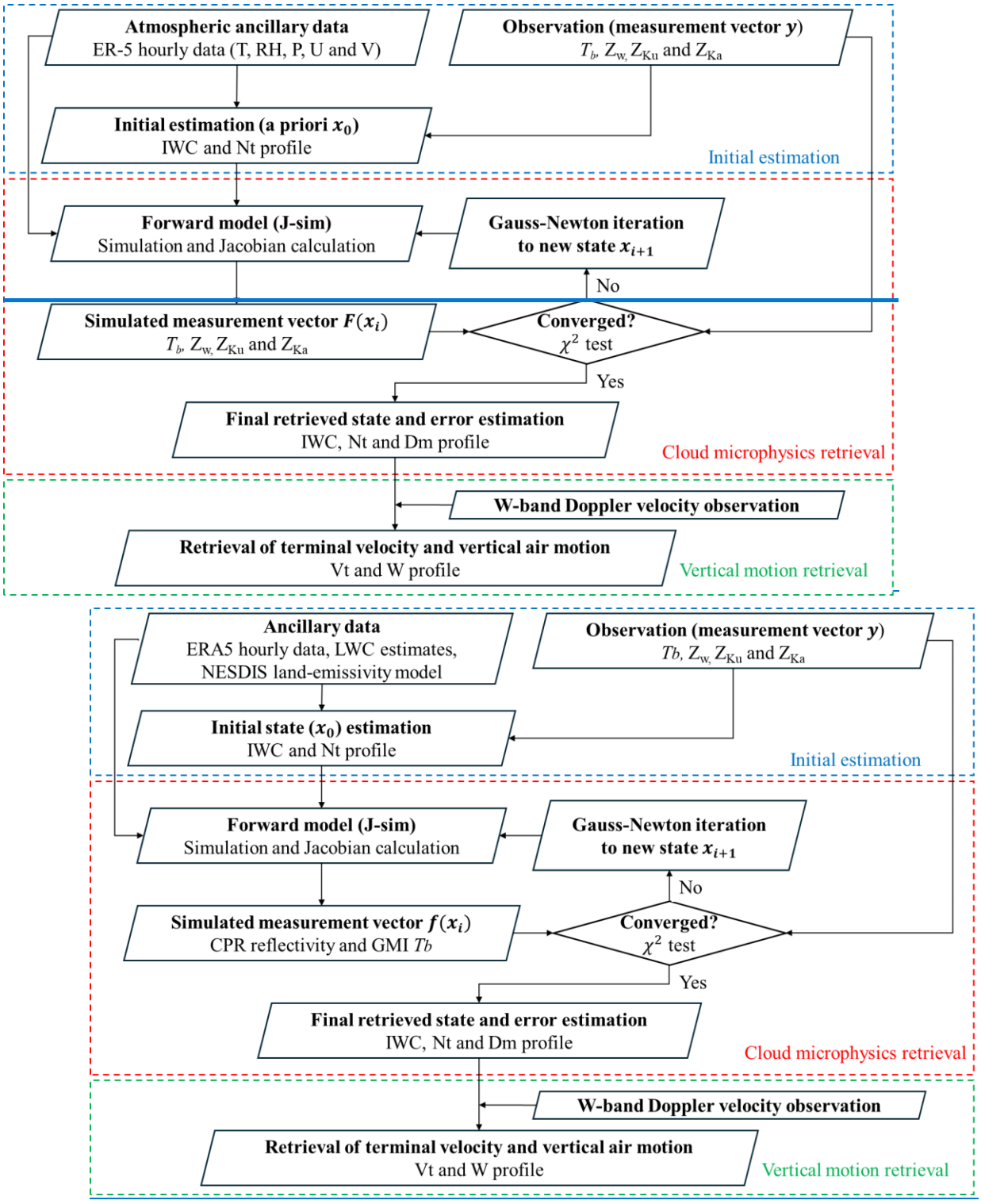
Atmospheric ancillary data
ER-5 hourly data (T, RH, P, U and V)
Observation (measurement vector y)
T_b, Z_w, Z_{Ku} and Z_{Ka}
Initial estimation (a priori x_0)
IWC and Nt profile
Initial estimation
Forward model (J-sim)
Simulation and Jacobian calculation
Gauss-Newton iteration
to new state x_{i+1}
No
Simulated measurement vector $F(x_i)$
T_b, Z_w, Z_{Ku} and Z_{Ka}
Converged?
χ^2 test
Yes
Final retrieved state and error estimation
IWC, Nt and Dm profile
Cloud microphysics retrieval
W-band Doppler velocity observation
Retrieval of terminal velocity and vertical air motion
Vt and W profile
Vertical motion retrieval
Ancillary data
ERA5 hourly data, LWC estimates,
NESDIS land-emissivity model
Observation (measurement vector y)
Tb, Z_w, Z_{Ku} and Z_{Ka}
Initial state (x_0) estimation
IWC and Nt profile
Initial estimation
Forward model (J-sim)
Simulation and Jacobian calculation
Gauss-Newton iteration
to new state x_{i+1}
No
Simulated measurement vector $f(x_i)$
CPR reflectivity and GMI Tb
Converged?
χ^2 test
Yes
Final retrieved state and error estimation
IWC, Nt and Dm profile
Cloud microphysics retrieval
W-band Doppler velocity observation
Retrieval of terminal velocity and vertical air motion
Vt and W profile
Vertical motion retrieval

Figure 4: Flow of the combined retrieval algorithm using multi-band radar and radiometer measurements. The blue dashed box denotes the initial-value estimation flow. The red dashed box indicates the optimal-estimation retrieval flow for cloud microphysical parameters (IWC, N_t and D_m). The part marked by green dashed box estimates V_d and W.

3.2 Cloud microphysical assumption

The particle size distribution (PSD) is one of the key microphysical properties that governs both bulk cloud physical quantities (Eqs. (1)–(3)) and the microwave scattering characteristics. In many previous studies, the PSD has been commonly approximated using analytical functions such as exponential, gamma, or lognormal distributions for computational convenience (Austin et al., 2009; Deng, M., G. G. Mace, Z. Wang, and H. Okamoto, 2010). Ice particles gradually grow as they fall through the cloud, evolving from small pristine crystals into larger aggregates, snowflakes, or graupel through processes such as vapor deposition, aggregation, and riming. To account for this vertical growth, several studies have introduced temperature-dependent PSD formulations (Austin et al., 2009; Heymsfield and Schmitt, 2013). Following O25, the present study assumes the temperature-dependent gamma PSD proposed by Heymsfield and Schmitt (2013) expressed as

$$\begin{aligned} N(D) &= N_0 D^{\mu} \exp(-\lambda D) \\ \mu &= -14.09 - 0.248\,T \ (T < -61\ [^{\circ}\mathrm{C}]), \\ \mu &= -0.59 - 0.030\,T \ \ (T \geq -61\ [^{\circ}\mathrm{C}]) \end{aligned} \tag{8}$$

Here N_0 is the intercept parameter, μ is the dispersion parameter, λ is the slope parameter, and D denotes the maximum particle dimension. In the retrieval framework, μ is assumed as a function of air temperature (T) according to Eq. (8), while N_0 and λ are free parameters to be optimized in the algorithm.

Another key microphysical property is the particle habit. In the present retrieval framework, the particle habit is prescribed in advance instead of being treated as a retrievable parameter. The particle habit assumption strongly affects both the ~~bulk~~ microphysical relationships, such as the mass–dimension *m(D)* and area-ratio A_r *(D)* relationships, and the microwave single-scattering properties (SSPs). Selecting an appropriate particle habit is essential for achieving accurate ice-hydrometeor retrievals. In previous studies, the *m(D)* and A_r *(D)* relationships for various particle models have commonly been expressed in power-law form, $m(D) = aD^b$ and $A_r(D) = \alpha D^{\beta}$, with the coefficients ($a, b, \alpha,$ and β) varying according to the assumed habit (Eriksson et al., 2018; Heymsfield and Schmitt, 2013; Liu, 2008). While SSPs for spherical particles can be computed exactly using Mie theory, the SSPs of nonspherical particles in the microwave regime are typically obtained from precomputed databases generated using the Discrete Dipole Approximation (DDA)(Draine and Flatau, 1994; Liu, 2008; Okamoto, 2002).

Table 4 lists the power-law coefficients ($a, b, \alpha,$ and β) of *m(D)* and *Ar (D)* for each particle habit assumed in this study. The total of 13 particle-habit models are evaluated, consisting of (1) the soft-sphere model based on the *m(D)* and *Ar(D)* relationships reported by Heymsfield and Schmitt (2013), with SSPs computed using Mie theory; (2) 11 nonspherical particle

models from Liu (2008), each with distinct *m(D)*, *Ar (D)*, and DDA-derived SSPs; and (3) a temperature-dependent mixed-habit configuration described below. Whereas O25 assumed a single particle habit independent of environmental conditions, previous observational and laboratory studies have shown that the dominant ice-particle habit in nature is primarily controlled by temperature and secondarily by ice supersaturation. Under highly supersaturated conditions at temperatures below −40 °C, bullet rosettes are known to dominate (Bailey and Hallett, 2004, 2009), and aircraft observations have confirmed the prevalence of rosettes in cirrus at similar temperatures (Lawson et al., 2019). For temperatures above −40 °C, the habit distribution becomes increasingly complex. Bullet rosettes originating in upper levels may grow into plate-like polycrystals as they fall, while dendrite and sector snowflakes tend to dominate at temperatures warmer than −20 °C (Bailey and Hallett, 2009). Inspired by this physical background, this study defines a temperature-dependent mixed-habit configuration: bullet rosettes are assumed for all particles at temperatures below –40 °C, while the fraction of bullet rosettes (F_r) linearly decreases as the fraction of dendrite/sector snowflakes (F_s) increases with temperature between –40 °C and 0 °C. This mixing ratio (F_r and F_s) is expressed by the following equation.

$$\begin{aligned} F_r &= 1 \ (T \le -40\ [^\circ\mathrm{C}]) \\ F_r &= \frac{T}{-40} \ \ (-40 < T \le 0\ [^\circ\mathrm{C}]), \\ F_s &= 1 - F_r \end{aligned} \tag{9}$$

The impact of these habit assumptions on retrieval performance is discussed in Section 4.3.

Particle habit	a_m (cgs units)	b_m (cgs units)	α (cgs units)	β (cgs units)
Soft Sphere	0.~~0528~~00528	2.1	$0.288 + 6.913e^{-3}T + 8.09e^{-5}T^2$	$0.2026 + 9.681e^{-3}T + 1.19e^{-4}T^2$
Long column	0.034	3.0	Not defined	Not defined
Short column	0.1122	3.0	Not defined	Not defined
Block column	0. 2103	3.0	Not defined	Not defined
Thick plate	0.1064	3.0	Not defined	Not defined
Thin plate	0.0296	3.0	Not defined	Not defined
3-bullet rosette	0.005	2.16	0.125	-0.351
4-bullet rosette	0.0039	2.23	0.125	-0.351
5-bullet rosette	0.0049	2.23	0.125	-0.351

6-bullet rosette	0.0059	2.24	0.125	-0.351
Sector snowflakes	0.0011	1.54	0.261	-0.377
Dendrite snowflakes	0.0015	2.0	0.261	-0.377
Mixed rosette- snowflake habit depending on temperature	Depending on the mixing ratio in Eq. (9).	Depending on the mixing ratio in Eq. (9).	Depending on the mixing ratio in Eq. (9).	Depending on the mixing ratio in Eq. (9).

Table 4: Power-law coefficients for the mass–dimension *m(D)* and area ratio *Ar(D)* relationships associated with the ice-particle habits used in this study. The coefficients for the soft-sphere model are taken from Heymsfield and Schmitt (2013), while those for the other nonspherical particle models are taken from Liu (2008). For the column-like and plate-like nonspherical models, α and β are not defined because no reported values are available. The unit of temperature T is °C.

3.3 Synergistic cloud microphysics retrieval using multi-band radars and radiometer

This subsection describes the retrieval algorithm illustrated in Fig. 4. The first step, marked by the blue dashed box in Fig. 4, corresponds to the initial estimation. In O25, the initial values of cloud-ice profiles were estimated using a machine-learning approach trained on reference data derived from a cloud-resolving model, the Nonhydrostatic ICosahedral Atmospheric Model (NICAM), over tropical oceans. Simulated satellite observations from the reference data using J-sim were used as input to the machine-learning system. This was proved to be a workable approach but is limited by the model performance such as the extent to which simulated cloud properties represent the variability in nature. In this study, the training strategy is modified and simplified. First, a wide range of cloud temperatures and IWC values are prescribed, and the corresponding Z_w is simulated using the forward model (J-sim). Because a temperature-dependent gamma PSD with parameters $\mu(T)$ and $\lambda(T)$ are assumed here (Heymsfield and Schmitt, 2013), the Z_w–IWC relationship depends on the cloud temperature. Using this dataset, a regression model is trained to predict IWC from Z_w and cloud temperature. Once IWC is retrieved, the associated N_t can be diagnosed from the $\mu(T)$ and $\lambda(T)$. Applying this method to observed Z_w profiles from CRS and temperature profiles from the ERA5 hourly reanalysis provides initial guess of the vertical profiles of IWC and N_t. However, this initial estimation still contains errors arising from signal attenuation of $Z_w$within the cloud and the assumption that λ depends solely on temperature. These errors are corrected within OE framework in the second step of the algorithm, shown in the red dashed box of Fig. 4. In this step, Z_w attenuation is explicitly accounted for, and λ is treated as a free parameter.

In the OE framework, the initial profiles of IWC and N_t are optimized by using CRS Z_w, CoSMIR T_b, HIWRAP Z_{Ku} and Z_{Ka}. The details of the OE implementation are based on the theoretical background given by Rodgers, (2000) as described in O25. This subsection provides a brief overview and modifications introduced in this study. The vertical distribution of ice-phase hydrometeors to be retrieved is represented by the state vector $\boldsymbol{X}$, and the observational inputs are represented by the

measurement vector $\boldsymbol{Y}$. The retrieval problem is expressed as the maximization of the posterior probability density function $p_{post}(\boldsymbol{X}|\boldsymbol{Y})$, which is equivalent to minimizing the cost function shown in Eq. (11) under the assumption of Gaussian probability density function.

$$\boldsymbol{X} = \begin{pmatrix} \log(IWC)_1 \\ \vdots \\ \log(IWC)_n \\ \log(N_t)_1 \\ \vdots \\ \log(N_t)_n \end{pmatrix}, \quad \boldsymbol{Y} = \begin{pmatrix} Z_{W_1} \\ \vdots \\ Z_{w_n} \\ T_{b_{89}} \\ \vdots \\ T_{b_{183\pm3}} \\ Z_{Ku_1} \\ \vdots \\ Z_{Ku_n} \\ Z_{Ka_1} \\ \vdots \\ Z_{Ka_n} \end{pmatrix}, \tag{10}$$

$$J = \left(\boldsymbol{Y} - F(\boldsymbol{X})\right)^T \mathbf{S_e^{-1}} \left(\boldsymbol{Y} - F(\boldsymbol{X})\right) + (\boldsymbol{X} - \boldsymbol{X}_a)^T \mathbf{S_a^{-1}} (\boldsymbol{X} - \boldsymbol{X}_a)\,, \tag{11}$$

The state vector $\boldsymbol{X}$ contains the vertical profiles of IWC and N_t, where n denotes the number of cloud layers. In O25, the measurement vector $\boldsymbol{Y}$ consisted only of the T_b and Z_w vertical profiles, whereas the vertical profiles of Z_{Ku} and Z_{Ka} are additionally included in this study. $\boldsymbol{F}(\boldsymbol{X})$ is the simulated measurement vector (T_b, Z_w, Z_{Ku}, Z_{Ka}) from the state vector $\boldsymbol{X}$ using a forward model (J-sim). The a priori state vector $\boldsymbol{X_a}$ corresponds to the initial estimate of the ice profile, and the error covariance matrices $\mathbf{S_a}$ and $\mathbf{S_e}$ are defined in the same manner as in O25. Details of the specifications of $\mathbf{S_a}$ and $\mathbf{S_e}$ are described in Section 3.3 of O25.

The cost function is minimized iteratively using the Gauss–Newton method Eq. (12).

$$\boldsymbol{X_{i+1}} = \boldsymbol{X_i} + \left(\mathbf{S_a^{-1}} + \mathbf{H_i^T S_e^{-1} H_i}\right)^{-1} \left[\mathbf{H_i^T S_e^{-1}} \left(\boldsymbol{Y} - \boldsymbol{F}(\boldsymbol{X_i})\right) - \mathbf{S_a^{-1}} (\boldsymbol{X_i} - \boldsymbol{X_a})\right], \tag{12}$$

$$\mathbf{H_i} = \begin{pmatrix} \frac{\partial Z_{w_1}}{\partial IWC_0} & \cdots & \frac{\partial Z_{w_1}}{\partial IWC_n} & \frac{\partial Z_{w_1}}{\partial Nt_0} & \cdots & \frac{\partial Z_{w_1}}{\partial Nt_n} \\ \vdots & \ddots & \vdots & \vdots & \ddots & \vdots \\ \frac{\partial Z_{w_n}}{\partial IWC_0} & \cdots & \frac{\partial Z_{w_n}}{\partial IWC_n} & \frac{\partial Z_{w_n}}{\partial Nt_0} & \cdots & \frac{\partial Z_{w_n}}{\partial Nt_n} \\ \frac{\partial Tb_{89}}{\partial IWC_0} & \cdots & \frac{\partial Tb_{89}}{\partial IWC_n} & \frac{\partial Tb_{89}}{\partial Nt_0} & \cdots & \frac{\partial Tb_{89}}{\partial Nt_n} \\ \vdots & \ddots & \vdots & \vdots & \ddots & \vdots \\ \frac{\partial Tb_{183}}{\partial IWC_0} & \cdots & \frac{\partial Tb_{183}}{\partial IWC_n} & \frac{\partial Tb_{183}}{\partial Nt_0} & \cdots & \frac{\partial Tb_{183}}{\partial Nt_n} \\ \frac{\partial Z_{Ka_1}}{\partial IWC_0} & \cdots & \frac{\partial Z_{Ka_1}}{\partial IWC_n} & \frac{\partial Z_{Ka_1}}{\partial Nt_0} & \cdots & \frac{\partial Z_{Ka_1}}{\partial Nt_n} \\ \vdots & \ddots & \vdots & \vdots & \ddots & \vdots \\ \frac{\partial Z_{Ka_n}}{\partial IWC_0} & \cdots & \frac{\partial Z_{Ka_n}}{\partial IWC_n} & \frac{\partial Z_{Ka_n}}{\partial Nt_0} & \cdots & \frac{\partial Z_{Ka_n}}{\partial Nt_n} \\ \frac{\partial Z_{Ku_1}}{\partial IWC_0} & \cdots & \frac{\partial Z_{Ku_1}}{\partial IWC_n} & \frac{\partial Z_{Ku_1}}{\partial Nt_0} & \cdots & \frac{\partial Z_{Ku_1}}{\partial Nt_n} \\ \vdots & \ddots & \vdots & \vdots & \ddots & \vdots \\ \frac{\partial Z_{Ku_n}}{\partial IWC_0} & \cdots & \frac{\partial Z_{Ku_n}}{\partial IWC_n} & \frac{\partial Z_{Ku_n}}{\partial Nt_0} & \cdots & \frac{\partial Z_{Ku_n}}{\partial Nt_n} \end{pmatrix}, \begin{pmatrix} \frac{\partial Z_{w_1}}{\partial \log(IWC_0)} & \cdots & \frac{\partial Z_{w_1}}{\partial \log(IWC_n)} & \frac{\partial Z_{w_1}}{\partial \log(Nt_0)} & \cdots & \frac{\partial Z_{w_1}}{\partial \log(Nt_n)} \\ \vdots & \ddots & \vdots & \vdots & \ddots & \vdots \\ \frac{\partial Z_{w_n}}{\partial \log(IWC_0)} & \cdots & \frac{\partial Z_{w_n}}{\partial \log(IWC_n)} & \frac{\partial Z_{w_n}}{\partial \log(Nt_0)} & \cdots & \frac{\partial Z_{w_n}}{\partial \log(Nt_n)} \\ \frac{\partial Tb_{89}}{\partial \log(IWC_0)} & \cdots & \frac{\partial Tb_{89}}{\partial \log(IWC_n)} & \frac{\partial Tb_{89}}{\partial \log(Nt_0)} & \cdots & \frac{\partial Tb_{89}}{\partial \log(Nt_n)} \\ \vdots & \ddots & \vdots & \vdots & \ddots & \vdots \\ \frac{\partial Tb_{183}}{\partial \log(IWC_0)} & \cdots & \frac{\partial Tb_{183}}{\partial \log(IWC_n)} & \frac{\partial Tb_{183}}{\partial \log(Nt_0)} & \cdots & \frac{\partial Tb_{183}}{\partial \log(Nt_n)} \\ \frac{\partial Z_{Ka_1}}{\partial \log(IWC_0)} & \cdots & \frac{\partial Z_{Ka_1}}{\partial \log(IWC_n)} & \frac{\partial Z_{Ka_1}}{\partial \log(Nt_0)} & \cdots & \frac{\partial Z_{Ka_1}}{\partial \log(Nt_n)} \\ \vdots & \ddots & \vdots & \vdots & \ddots & \vdots \\ \frac{\partial Z_{Ka_n}}{\partial \log(IWC_0)} & \cdots & \frac{\partial Z_{Ka_n}}{\partial \log(IWC_n)} & \frac{\partial Z_{Ka_n}}{\partial \log(Nt_0)} & \cdots & \frac{\partial Z_{Ka_n}}{\partial \log(Nt_n)} \\ \frac{\partial Z_{Ku_1}}{\partial \log(IWC_0)} & \cdots & \frac{\partial Z_{Ku_1}}{\partial \log(IWC_n)} & \frac{\partial Z_{Ku_1}}{\partial \log(Nt_0)} & \cdots & \frac{\partial Z_{Ku_1}}{\partial \log(Nt_n)} \\ \vdots & \ddots & \vdots & \vdots & \ddots & \vdots \\ \frac{\partial Z_{Ku_n}}{\partial \log(IWC_0)} & \cdots & \frac{\partial Z_{Ku_n}}{\partial \log(IWC_n)} & \frac{\partial Z_{Ku_n}}{\partial \log(Nt_0)} & \cdots & \frac{\partial Z_{Ku_n}}{\partial \log(Nt_n)} \end{pmatrix}, \tag{13}$$

The Jacobian matrix $\mathbf{H_i}$, which represents the sensitivity of each observation to perturbations in IWC and N_t at each layer, is computed by repeated forward simulations and is updated each time the state vector is updated. The iterations are continued until the χ^2convergence criterion of Rodgers (2000) is satisfied, yielding the final retrieved state vector $\boldsymbol{X_{fin}}$. The uncertainty of the retrieval is then calculated from the final Jacobian matrix $\mathbf{H_{fin}}$ using Eq. (14).

$$\mathbf{S} = \left(\mathbf{S_a^{-1}} + \mathbf{H_{fin}^T S_e^{-1} H_{fin}}\right)^{-1}. \tag{14}$$

Using the retrieved IWC and N_t together with $\mu(T)$ assumed in Eq. (8), the PSD can be diagnosed as $N_{\mathrm{ret}}(D)$. For the comparison with probe measurements, $N_{\mathrm{ret}}(D)$ is substituted into Eqs. (1)–(7) to calculate the cloud microphysical parameters (IWC, N_t, D_m, and V_t) for particles larger than 100 μm to ensure consistency with the probe data. Here, the $m(D)$ and $A_r(D)$ relationships use the coefficients corresponding to the assumed particle habit (Table 4). Finally, the vertical air motion W is estimated by subtracting the retrieved terminal fall velocity V_t from the observed Doppler velocity V_d.

3.3 Synergy expected by combined observation from microwave sensors

This subsection discusses qualitatively the differences in the scattering signals detected by the multiple microwave sensors used as inputs to the algorithm as well as the expected synergy effects. The observed high-frequency T_b by passive microwave radiometers are sensitive to the extinction (absorption and scattering) by ice hydrometeors, while radar reflectivity mainly reflects their backscattering properties. Figure 5 shows contour lines of the 13 GHz backscattering coefficient σ_{b13} (green),

the 94 GHz backscattering coefficient σ_{b94} (blue), and the 183±7 GHz extinction coefficient $\sigma_{e183\pm7}$ (orange), obtained by varying IWC and N_t over a wide range. The bullet-rosette particles are assumed here. In the upper-left part of the figure, all three coefficients exhibit nearly parallel contour patterns, indicating that the observed scattering information is largely redundant across sensors. In contrast, in the lower-right region—where IWC is large and N_t is small, meaning that the particle size becomes larger—the contour patterns differ substantially. In particular, the contour lines of the $\sigma_{e183\pm7}$ are nearly orthogonal to those of the σ_{b13} and σ_{b94} coefficients. This difference in contour patterns arises because 13 and 94 GHz wavelength remain within the Rayleigh-scattering regime for such particle sizes, while the shorter wavelength of 183 GHz interacts with the particles in Mie-scattering regime.

The near orthogonality of the two contours indicate that measurements from the two sensors carry independent information in retrieving N_t and IWC simultaneously (Pfreundschuh et al., 2020). In our retrieval framework, these complementary sensitivities are explicitly incorporated through the Jacobian matrix $\mathbf{H_i}$ in Eq. (13) to optimize the state vector $\boldsymbol{X}$. For large ice hydrometeors, the combined use of radar and radiometer observations is expected to reduce the retrieval uncertainty in cloud microphysical properties that cannot be constrained by single sensor.

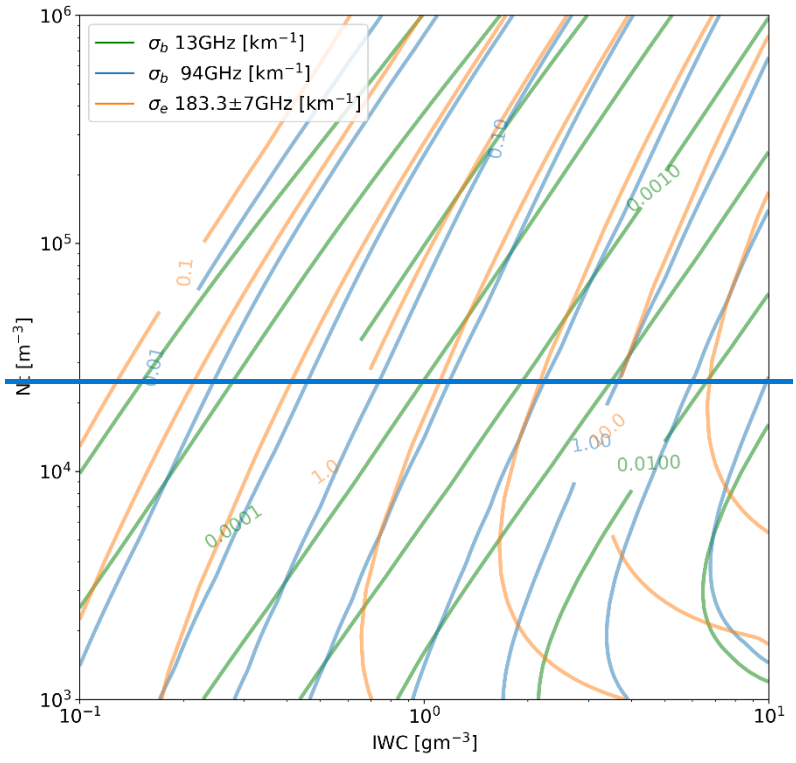

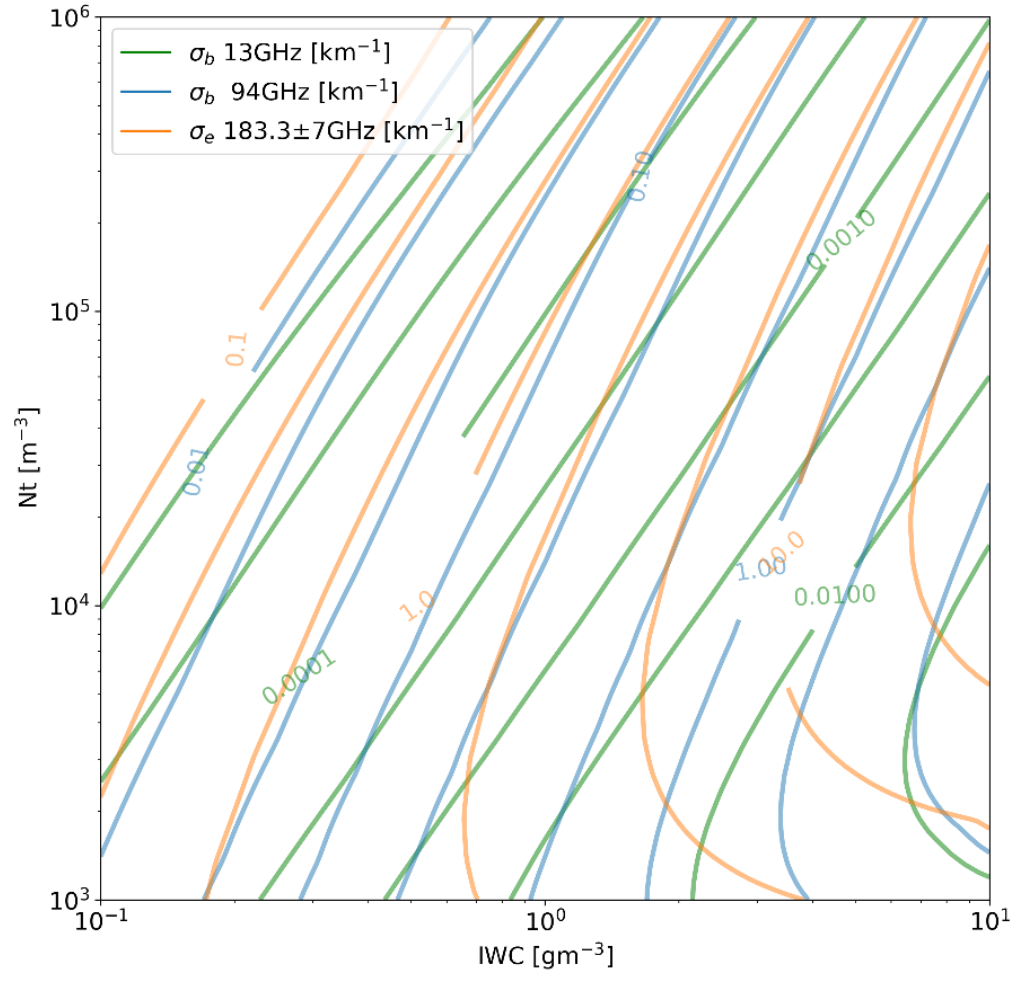

Figure 5: Sensitivity of the 13 GHz backscattering coefficient σ_{b13} (green), the 94 GHz backscattering coefficient σ_{b94} (blue), and the 183±7 GHz extinction coefficient $\sigma_{e183\pm7}$ (orange).

4 Results

4.1 Validation of cloud microphysical parameters

In this section, the performance of the retrieval algorithm is assessed through a comparison with in situ observations. Figures 6a-c show the retrieved vertical cross-sections of IWC, N_t, and D_m for the deep stratiform snowfall event over land on 5 February 2020 listed in Table 1. The retrieval was conducted under the assumption of a mixed rosette–snowflake particle habit as described in Sect. 3.2. The dashed line in each panel indicates the 0 °C level, and the solid gray line marks the flight altitude of the P-3 aircraft carrying the probe instruments, enabling a direct comparison at this altitude. Figures 6d-f show the

comparison between the retrieved values (orange) and the probe observations (blue) of IWC, N_t, and D_m. Overall, the retrieved values exhibit good agreement with the in situ probe measurements in magnitude and variability.

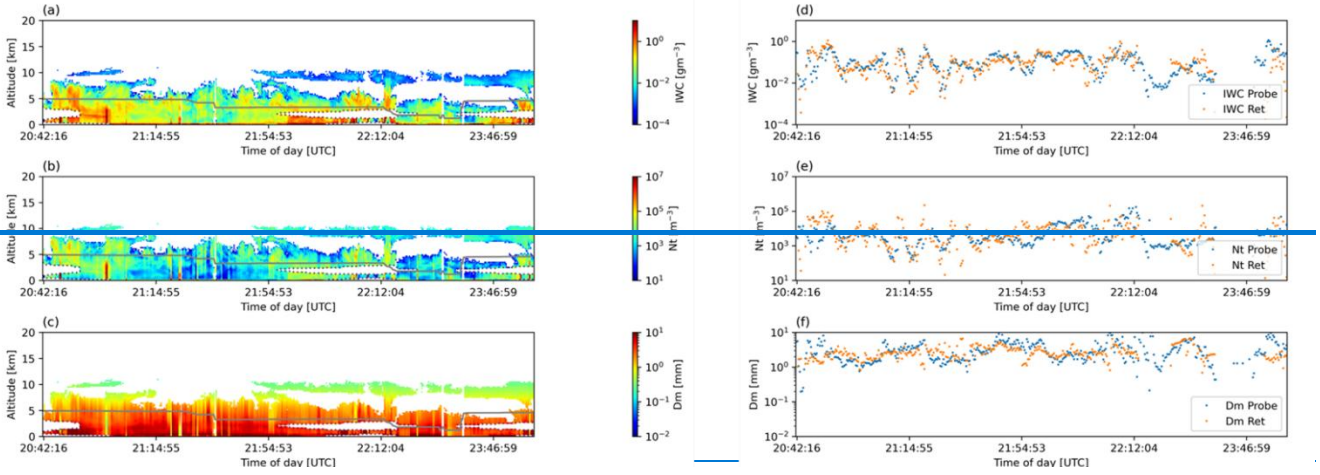

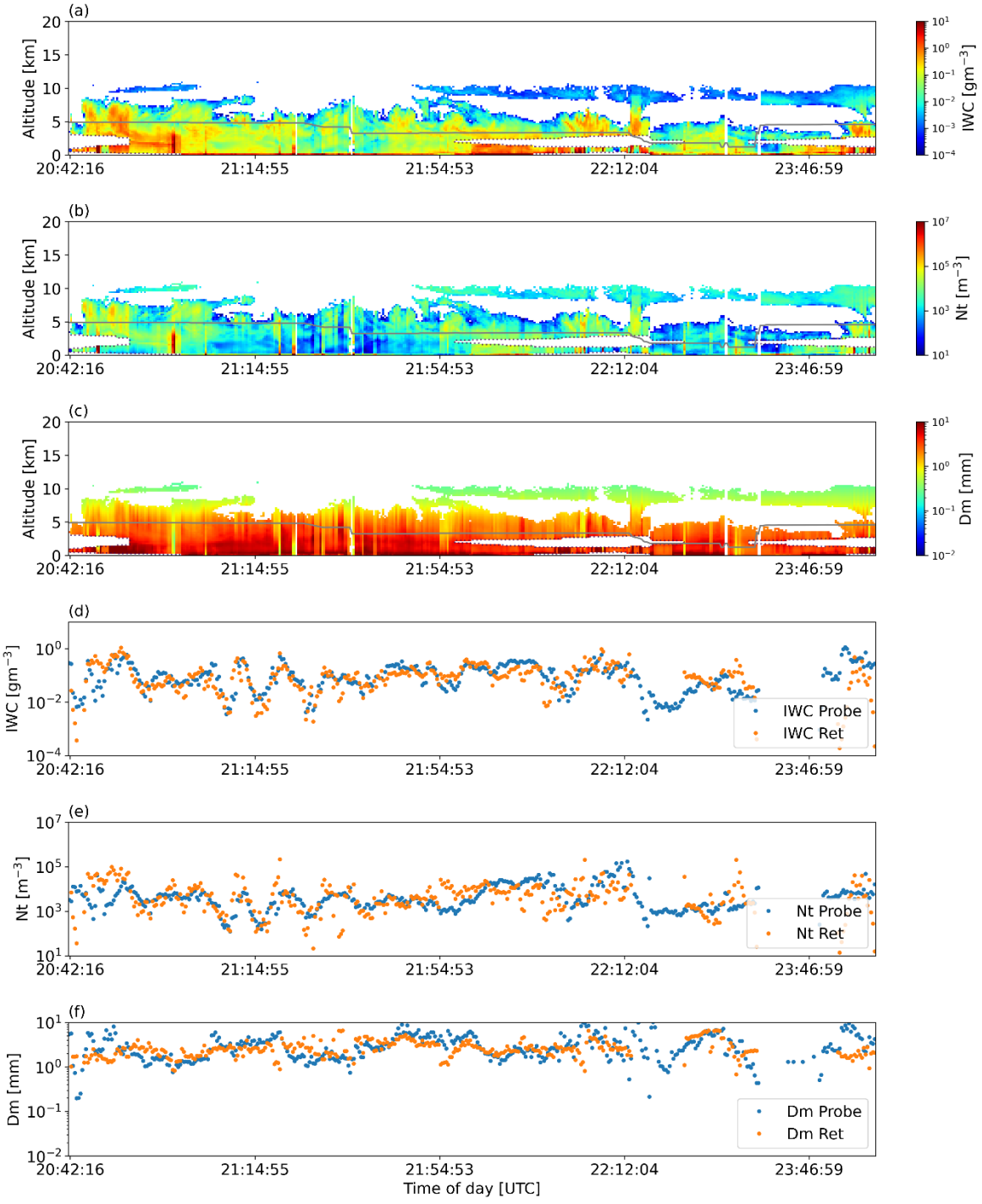

Figure 6: Comparison between the retrieved values and in situ probe measurements for the deep stratiform snowfall event over land on 5 February 2020. The retrieved vertical profiles of (a) IWC, (b) N_t, and (c) D_m. Comparisons between the retrieved values (orange) and probe measurements (blue) of (f) IWC, (g) N_t, and (h) D_m at the P-3 aircraft flight altitude (gray lines in (a)–(c)).

Figure 7 is as Fig. 6 but for the deep convective rainfall case over ocean on 25 January 2020 shown in Fig. 2. In this case, a consistent bias is evident between 19:20 and 19:26 UTC while the overall variability is still captured. ~~One possible reason for these biases may be strong updrafts. CRS Doppler measurements in Fig. 2b show strong updrafts between 19:20 and 19:24 UTC and weak updrafts between 19:24 and 19:26 UTC, roughly coincident with a pronounced enhancement of IWC and N_t in Figs. 7a–b. Strong updrafts imply active convection and hence a marked non-uniform beam filling effect due to the patchiness of convective clouds, which can undermine the retrieval accuracy. Another possible reason is that~~One possible explanation for this bias is that the in-situ measurements were obtained near the cloud base or cloud edges, where the influence of spatiotemporal mismatch is more substantial. Another possible explanation is that the bias arises from assumptions regarding particle habit and other microphysical properties. For example, the assumed mixed rosette–snowflake habit, where rosette particles formed in the upper layer fall and grow into snowflakes, may not be appropriate in updraft regions~~.~~ such as those in the cases shown in Figs. 2 and 7. Rather, snow and graupel particles formed at lower levels can be transported upward and mixed with particles generated aloft within an updraft. The impact of particle habit assumptions on retrieval accuracy will be discussed in the next section.

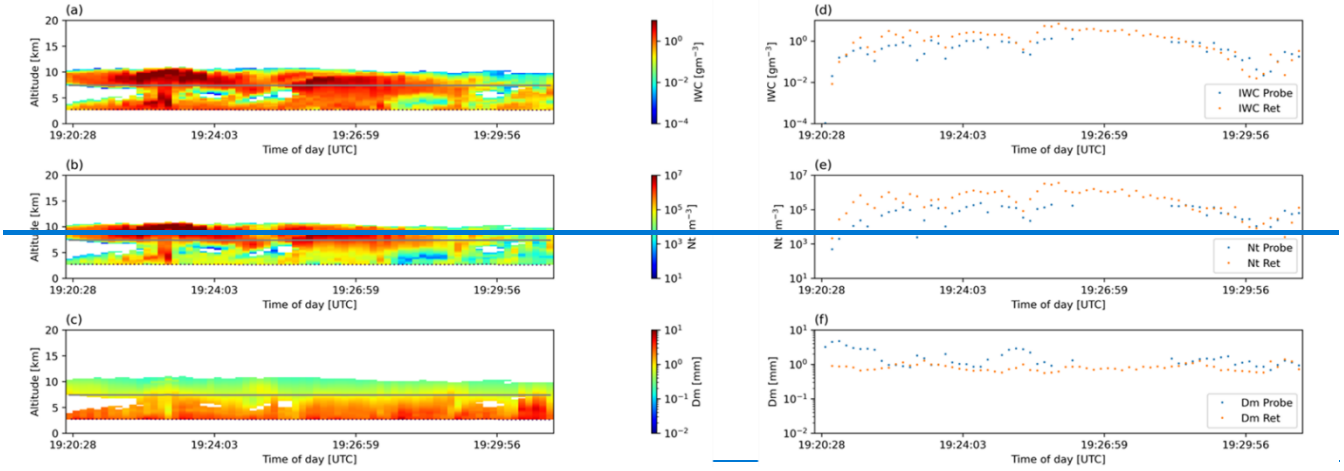

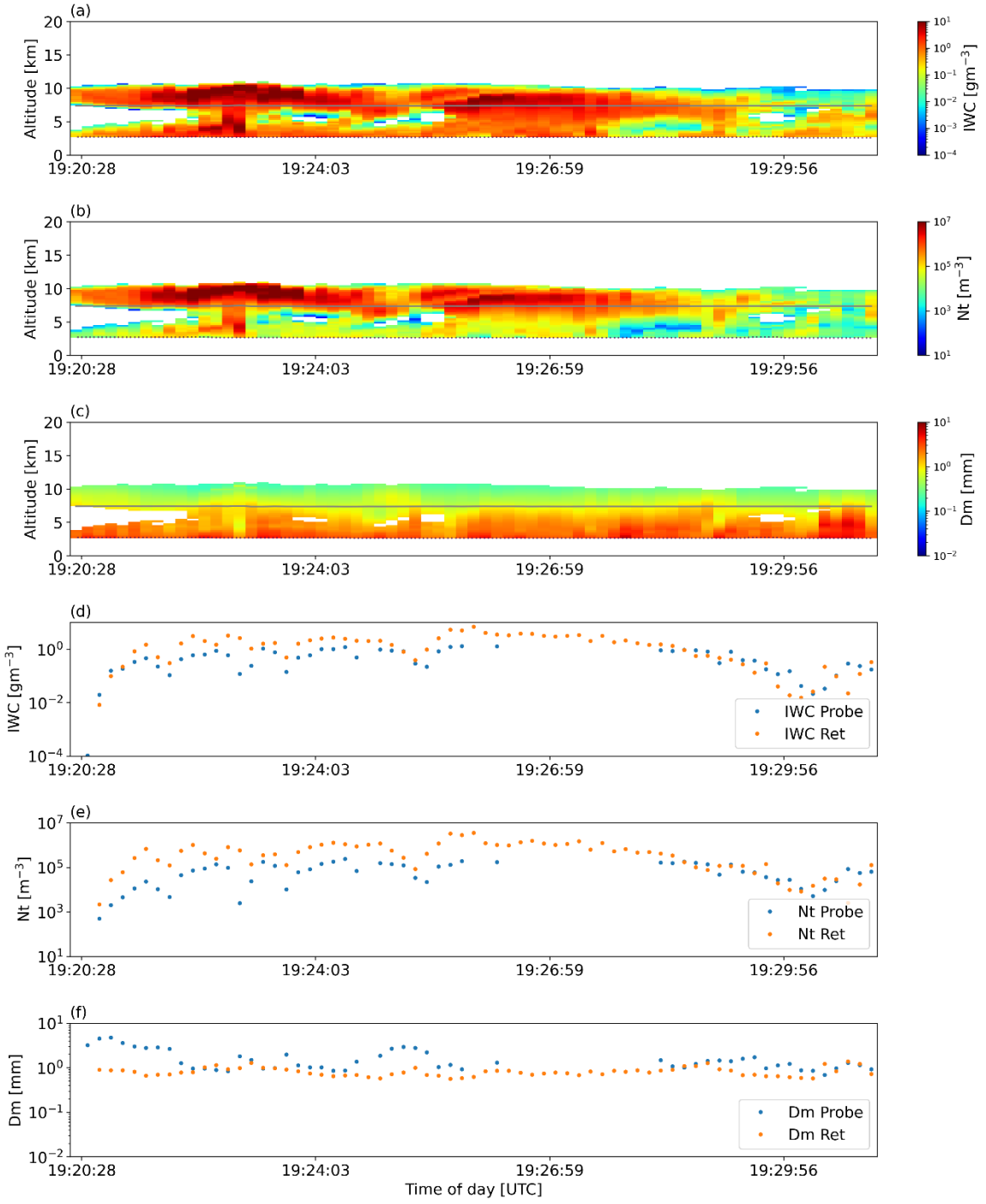

Figure 7: Same comparison as shown in Fig. 6, but for the deep convective rainfall case over the ocean on 25 January 2020

Figure 8 shows scatter plots comparing the retrieved values with the probe measurements for all cases listed in Table 1. Figures 8a-c correspond to the results for IWC, N_t, and D_m, respectively. The color scale indicates the number of data points contained in each bin. Although the scatter plots exhibit a considerable spread, mean bias relative to the probe data (in logarithmic scale) is small. The mean ratios of the retrieved values to the probe data are 1.01, 0.97, and 1.05 for IWC, N_t, and D_m, respectively. Deng et al. (2013) reported that the flight-mean ratios of retrieved IWC to in-situ values for the existing cloud-ice products 2C-ICE, DARDAR, and 2B-CWC-RVOD were 1.12, 1.59, and 1.02, and that the flight-mean ratios for the effective radius r_e were 1.05, 1.18, and 1.61, respectively. These values are comparable to the present results. Possible sources of the spread in Figs. 8a-c include ~~the slight mismatch of the observation time and locations and~~ differences in spatial resolution between the P-3 in situ probes and the ER-2 measurements as shown in Fig. 2b in addition to the uncertainties in assumptions (PSD and ice habit etc.) built in the algorithm. Additional sources of error may include uncertainties in the assumed water vapor and LWC estimates, as well as the temporal mismatch between the ER-2 and P-3 observations. However, supplementary analyses (see Supplement) indicate that these factors have a limited impact on the ice-hydrometeor retrieval accuracy for the IMPACTS cases.

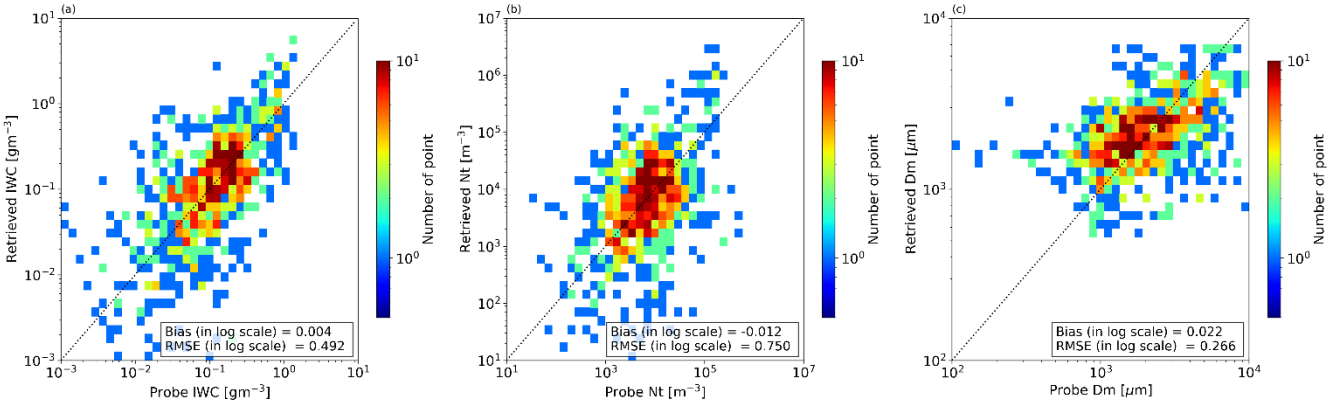

Figure 8: Evaluation of the combined retrieval accuracy. Statistical comparisons between the retrieved and in situ probe–measured values of (a) IWC, (b) N_t, and (c) D_m. The bias and RMSE on a logarithmic scale are shown in the upper-left corner of each panel.

4.2 Impacts of particle habit assumptions

The impact of the assumed ice particle habit on the retrieval accuracy is examined. Retrievals are performed repeatedly for each habit listed in Table 4 one after another, and the results are compared with the in-situ measurements in the same manner as in Fig. 8. Figure 9 summarizes the retrieval bias and RMSE for IWC, N_t, and D_m under each habit assumption. Uncertainties in particle habit assumptions can lead to retrieval biases of up to roughly two orders of magnitude in IWC and N_t. It is evident that the retrieval accuracy for IWC and N_t is higher for bullet rosettes, snowflakes, soft spheres, or the mixed rosette-snowflake habit particles (denoted as "-b ros", "-snow", "Sphere" and "Mix") than for column-like or plate-like particles (denoted as "-

col" and "-pl"). Among these, the mixed habit assumption provides the best performance overall. It should be noted that this conclusion is derived only from the cases observed during the IMPACTS field campaign. This mixed-habit assumption may not necessarily be appropriate for other cloud environments, for example, tropical convective systems in which strong updrafts could mix various type of ice particles originating from many different temperature layers. To address this limitation, future work will use a global satellite radar–radiometer matchup dataset (Turk et al., 2021; Aoki et al., 2025) to evaluate whether the same habit assumptions remain valid across different regions, seasons, and cloud types.

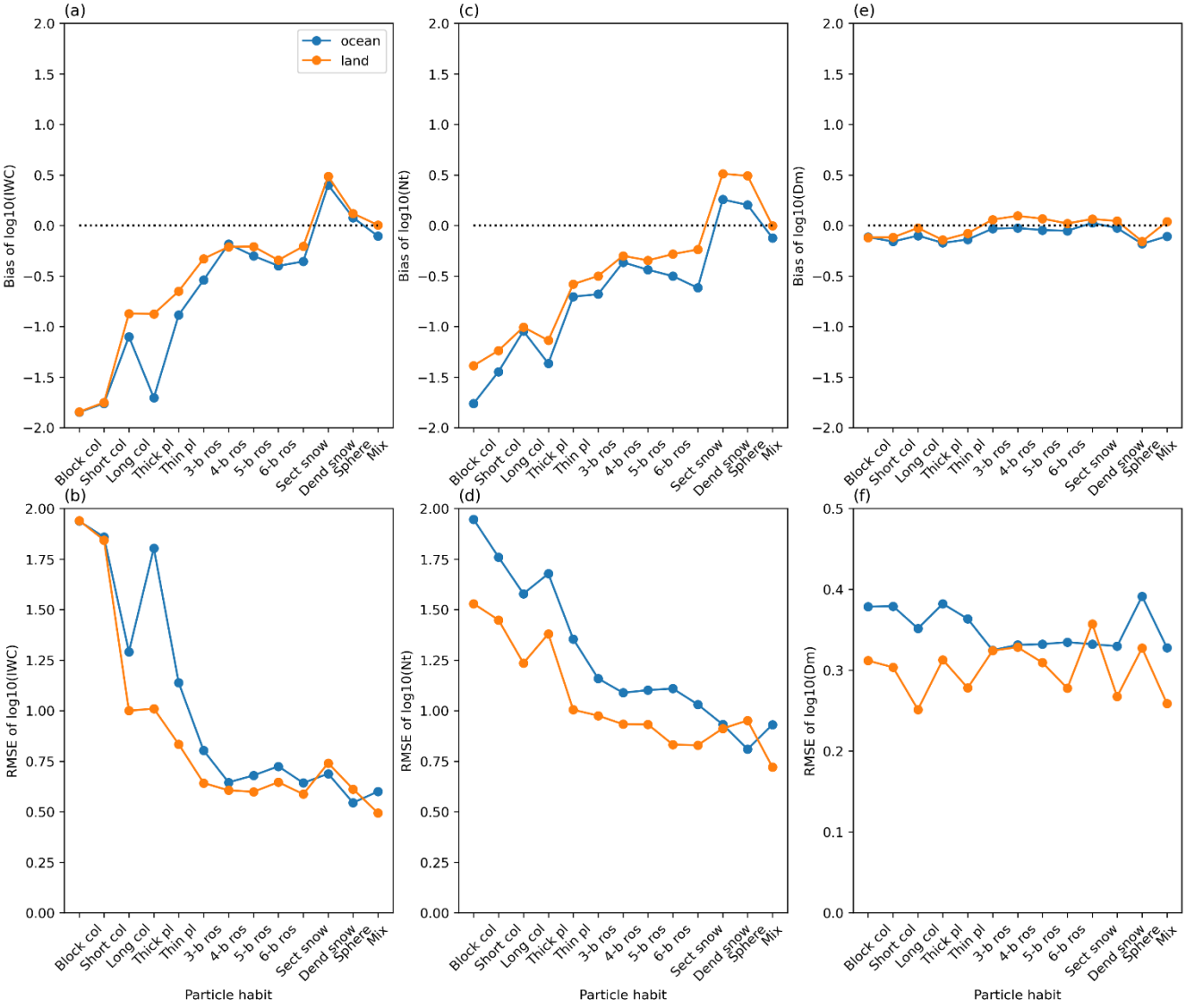

Figure 9: Retrieval accuracy (bias and RMSE) for each assumed particle model listed in Table 4. The column-like and plate-like particle habits are denoted as "–col'' and "–pl,'' respectively; bullet-rosette habits as "–b ros''; snowflake habits as "–snow''; the

soft-sphere model as "Sphere''; and the temperature-dependent mixed habit of rosettes and snowflakes as "Mix.'' The red lines represent results for all land cases, and the blue lines represent results for all ocean cases.

4.3 Consistency in measurement space

It is necessary to examine the self-consistency of the algorithm, that is, whether the synthetic observations simulated from the retrieved IWC, N_t, and D_m reproduce the actual ER-2 observations. Figure 10 compares the simulated and observed ER-2 measurements of CRS Z_w, CoSMIR high-frequency T_b, and HIWRAP Z_{Ka} and Z_{Ku} for all cases listed in Table 1. Only the solid-hydrometeor layers (temperatures below −3 °C) are used in the radar reflectivity comparison. The color scale indicates the number of samples within each bin. An excellent agreement is generally achieved for all sensors (CRS, CoSMIR, and HIWRAP). This result demonstrates that the algorithm is able to retrieve ice-hydrometeor profiles that are physically consistent with passive and active microwave observations over a wide frequency range from 13 to 183 GHz.

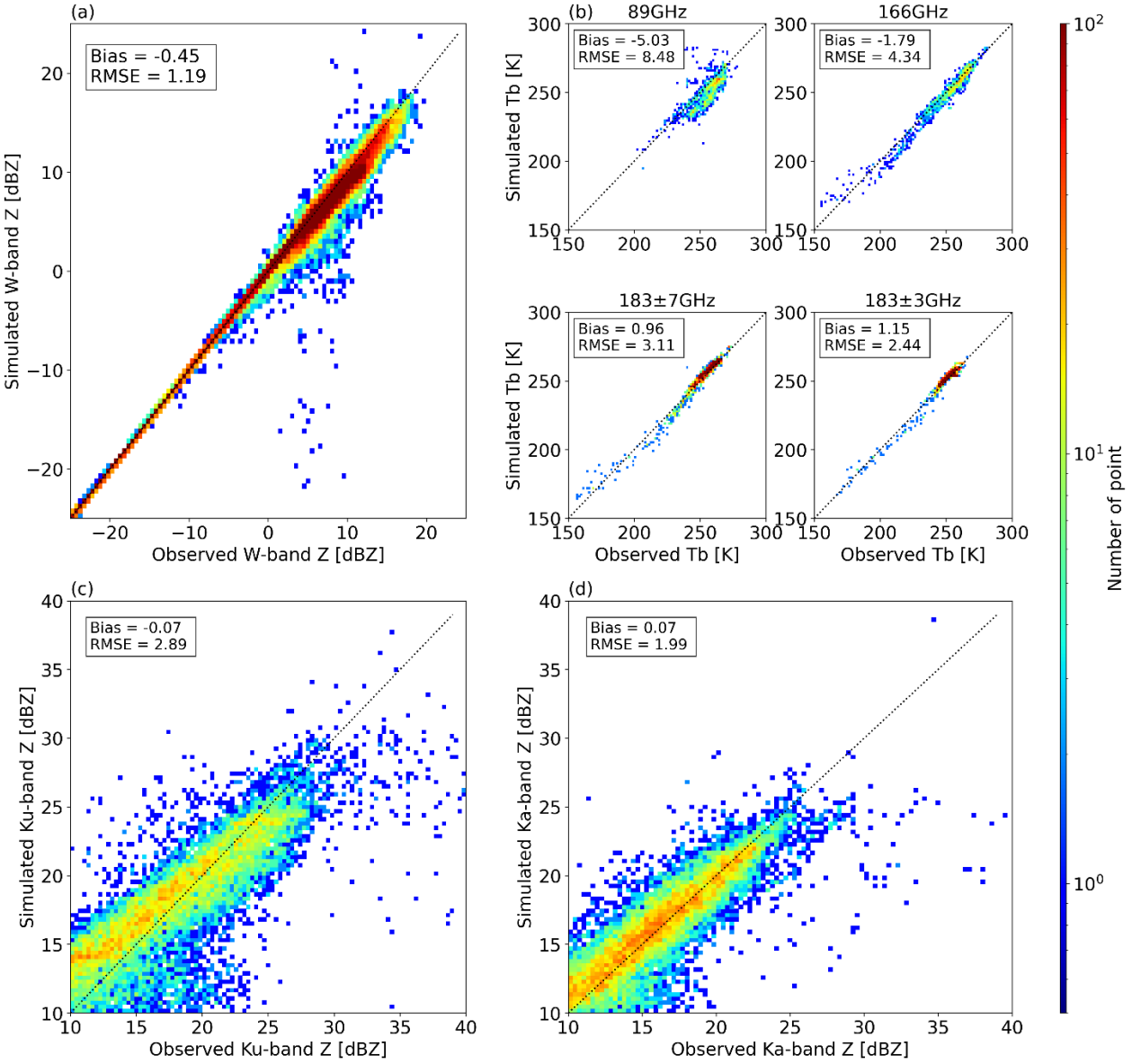

460 **Figure 10: Comparison between the radar reflectivity and brightness temperature from the ER-2 airborne sensors and the corresponding observations simulated from the retrieved ice-hydrometeor profiles using the forward model (J-sim). Retrievals assuming the mixed rosette–snowflake particle habit are used. (a) W-band radar reflectivity of CRS, (b) high-frequency brightness temperature of CoSMIR, (c) Ku-band radar reflectivity, and (d) Ka-band radar reflectivity of HIWRAP.**

465

While Fig. 9 shows that the mixed particle habit yields the best agreement with the in-situ measurements, an important scientific question is whether the available observations alone are sufficient to constrain particle habit. O25 demonstrated that

the simultaneous reproducibility of Z_w and high-frequency T_b depends on the assumed particle habit. It also showed that the uncertainty in particle habit can be effectively reduced particularly for tropical clouds with large IWP. However, for the IMPACTS cases, no clear differences in reproducibility were found among the different habit assumptions (shown in Supplement) unlike in O25. This finding suggests that, for midlatitude snowstorms, prescribing the particle habit assumption consistent with in situ observations may be a more effective approach than attempting to constrain it solely from remote sensing measurements. This issue will be further investigated in future work when extending the algorithm to a global framework including both tropical and midlatitude systems.

5 Discussion

5.1 Evaluation of terminal fall velocity

This section extends the evaluation to validate the Z_w-weighted terminal fall velocity (V_t) using not only the probe-measured PSD ($N_{probe}(D)$) but also area ratio distribution ($Ar_{probe}(D)$). This implies that agreement in terminal velocity requires not only consistency in the particle size distribution $N(D)$but also the validity of the assumed particle model $A_r(D)$. Since $N_{ret}(D)$ can be diagnosed from the retrieved IWC, N_t, and D_m, and the assumed particle model (Table 4) provides the $m(D)$ and $Ar(D)$ relationship, V_t can be computed for both the retrieval results and the probe measurements using Eqs. (4)-(7). Here, the cloud retrieved values assuming the mixed rosette–snowflake habit, which exhibited the best overall performance in Fig. 9, is used to calculate V_t for comparison with the probe measurements.

Figures 11a-c show the vertical profiles of the V_t diagnosed from the retrieved cloud parameters for the two cases presented in Figs. 6 and 7. The velocity is defined as upward positive. Near the cloud top, the terminal fall velocity approaches 0 m s^{-1} because the ice particles are small, whereas V_t increases as the particles grow larger in the deeper cloud layers. At the altitudes indicated by the gray lines, the retrieved V_t values are compared with the probe-measured V_t as shown in Figs. 11b and d. The comparison in Fig. 11b shows good agreement, while Fig. 11d exhibits biases in some regions. This is likely because the retrieval accuracy of IWC, N_t, and D_m —that is, of the diagnosed $N_{\mathrm{ret}}(D)$— is lower for the case in Fig. 7 (Fig. 11d) than for that in Fig. 6 (Fig. 11b). Figure 11e presents statistical comparisons of V_t for all observation cases. Both the retrieved and probe-measured $V_t$values are concentrated around 1 m s^{-1}, making the correlation difficult to evaluate, but the mean bias and RMSE is very small (−0.02 m s^{-1} and −0.30 m s^{-1}), indicating good overall agreement between the retrievals and probe measurement.

An additional validation ~~method~~ for V_t and vertical air motion W is also conducted using the Doppler velocity (V_d) observed by the CRS. Since Doppler measurements provide vertical profiles, they allow evaluations at various altitudes beyond a specific level as in the in-situ probe measurements. Figure 11f shows the histogram of the difference between the observed V_d and the

retrieved ~~terminal fall velocity~~ V_t~~. All the data from the solid-phase layers are used in this analysis, excluding the liquid-phase (rain) layers as identified by $V_d < -2$ m s^{-1}. In theory, this difference~~, which corresponds to ~~the~~ vertical air motion ~~(W).~~, in orange. For comparison, the histogram of observed V_d is shown in blue. Only solid-phase data (temperatures below −3 °C) are used. Since both updrafts and downdrafts are present, the mean and mode (i.e., the most frequent value) of W should ideally approach 0 m s^{-1} when a sufficient number of samples are available. ~~The~~ As shown in Fig. 11f, the mean value of V_d ~~$-V_t$ obtained~~ is ~~−0.08~~−0.092 m s^{-1}, whereas the mean value of W is 0.02 m s^{-1}, which is sufficiently ~~small compared to the typical magnitude of V_t (~1 m s^{-1}), and the mode is also~~ close to ~~0 m s^{-1}. These results indicate~~zero. This indicates that ~~the retrieved V_t values~~particle fall velocity and vertical air motion are ~~not only consistent with the in situ probe measurements but also~~ reasonably ~~consistent with~~separated from the Doppler velocity~~ observations.~~. The width of the W histogram (standard deviation) is slightly smaller than that of V_d, although the difference is small. This may suggest that the variability in V_d is primarily explained by variations in W rather than V_t, but it may also reflect limited accuracy in the estimation of V_t.

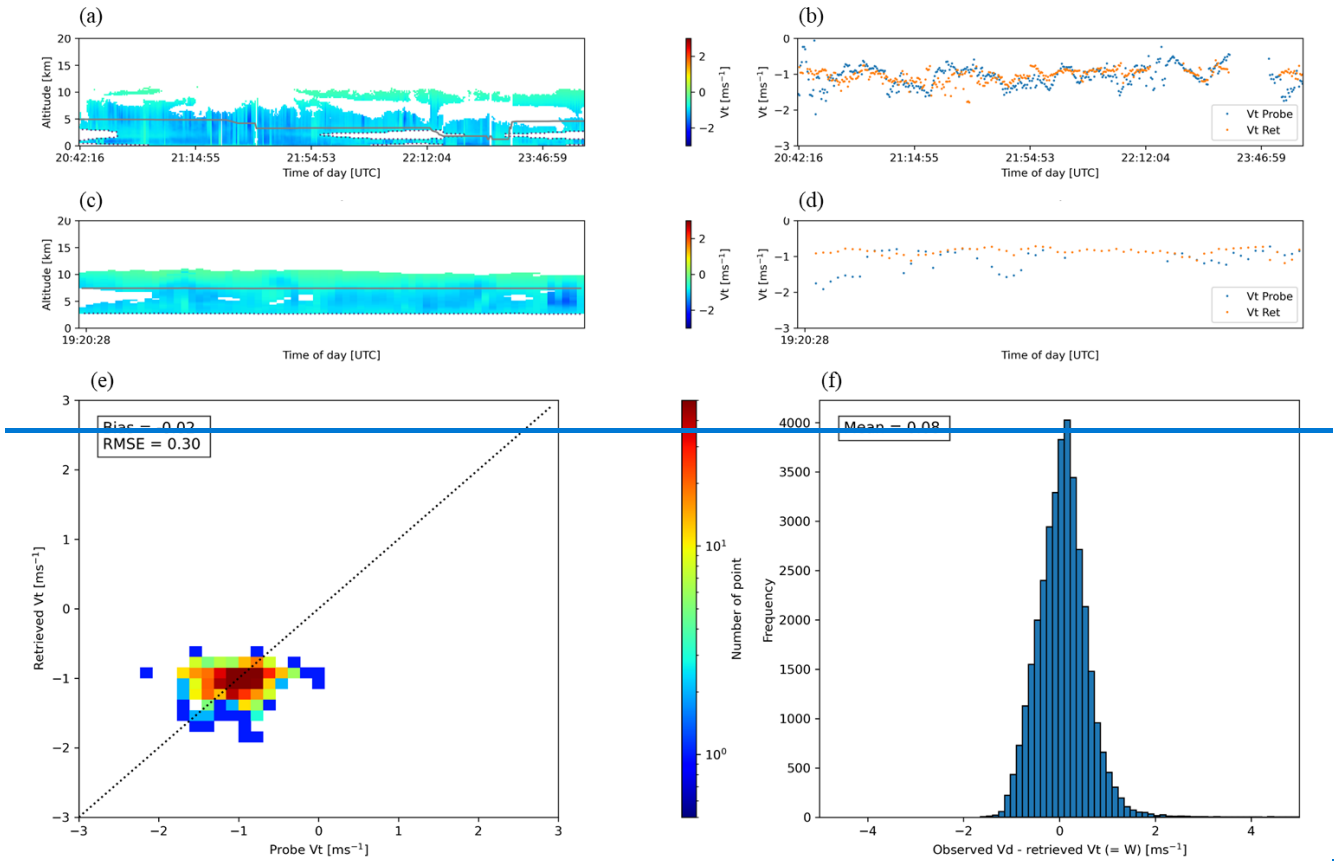

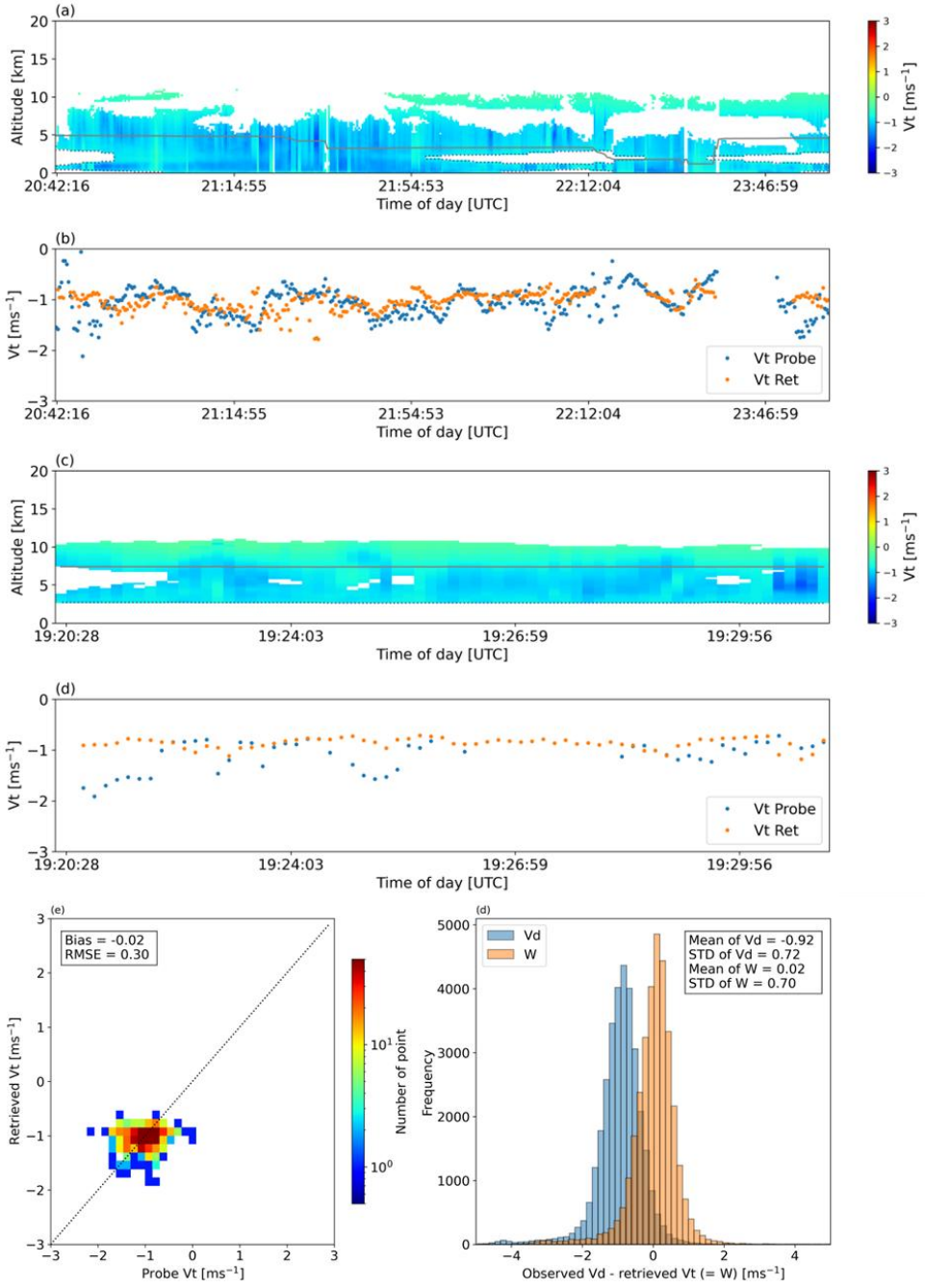

Figure 11 Evaluation of the retrieval accuracy for Z_w-weighted terminal fall velocity (V_t). (a) Vertical profiles of retrieved V_t and (b) comparison results between retrievals and probe measurements in the case shown in Fig. 6. (c) and (d) are same comparison as shown in (a) and (b), but for the case shown in Fig. 7. (e) Statistical comparison between retrieved and probe-measured V_t values across all cases. (f) Histogram of the difference between the CRS W-band Doppler velocity (V_d) and the retrieved V_t, corresponding to the vertical air motion W.

5.2 Benefit of combined use of multiple sensor observation

This section discusses the improvement in retrieval accuracy achieved by multiple microwave sensors employed in tandem. Figure 12 compares the probe measurements (black lines) with the retrievals obtained using Z_w only (blue), the combined use of Z_w and T_b (green), and the combined use of Z_w, T_b, Z_{Ku}, and Z_{Ka} (orange) for the land case on 25 January 2020. These retrievals are obtained by restricting the measurement vector $\boldsymbol{Y}$, Jacobian matrix $\boldsymbol{H}$, and measurement-error covariance matrix $\boldsymbol{S_e}$ (see Section 3.3) to contain the selected components only of Z_w, $Z_w + T_b$, and $Z_w + T_b + Z_{Ku} + Z_{Ka}$.

Retrievals using Z_w only (blue lines) exhibit noticeable biases relative to the probe observations. In particular, the retrieved D_m remains nearly constant and fails to reproduce the variations observed by the probe measurements. This is likely because, in the optimal estimation using Z_w only, the errors and uncertainties in the initial state $\boldsymbol{X_a}$ can hardly be corrected. ~~When~~In estimating ~~$\boldsymbol{X_a}$~~ X_a, attenuation effects are not considered, and the PSD parameters ~~μ and~~μ and λ are assumed to depend only on temperature~~, and~~. Therefore, the ~~D_m corresponding~~initial estimate contains errors due to ~~$\boldsymbol{X_a}$ is also determined solely by temperature. In addition, since $\boldsymbol{X_a}$ is already consistent with~~attenuation as well as uncertainties in the assumed PSD parameters. When only Z_w ~~through the forward model ($\boldsymbol{Y} = \boldsymbol{F}(\boldsymbol{X_a})$),~~is used in the ~~observational information from Z_w has no ability to update~~subsequent OE framework, attenuation-related errors can be corrected, whereas the ~~state vector $\boldsymbol{X}$ by~~uncertainty in λ assumed in the ~~Gauss–Newton iteration (Eq. 12).~~initial estimation cannot be effectively constrained. As a result, the retrieval accuracy of N_t and D_m remains limited when using Z_w alone. In contrast, when other microwave sensor observations are incorporated (green and orange lines), the retrieval accuracy for N_t and D_m improves in several regions (e.g., between 20:36 and 20:43 UTC or between 21:08 and 22:15 UTC). This improvement demonstrates that additional information from T_b, Z_{Ku} and Z_{Ka} effectively constrains the uncertainties in N_t and D_m that cannot be resolved by Z_w only.

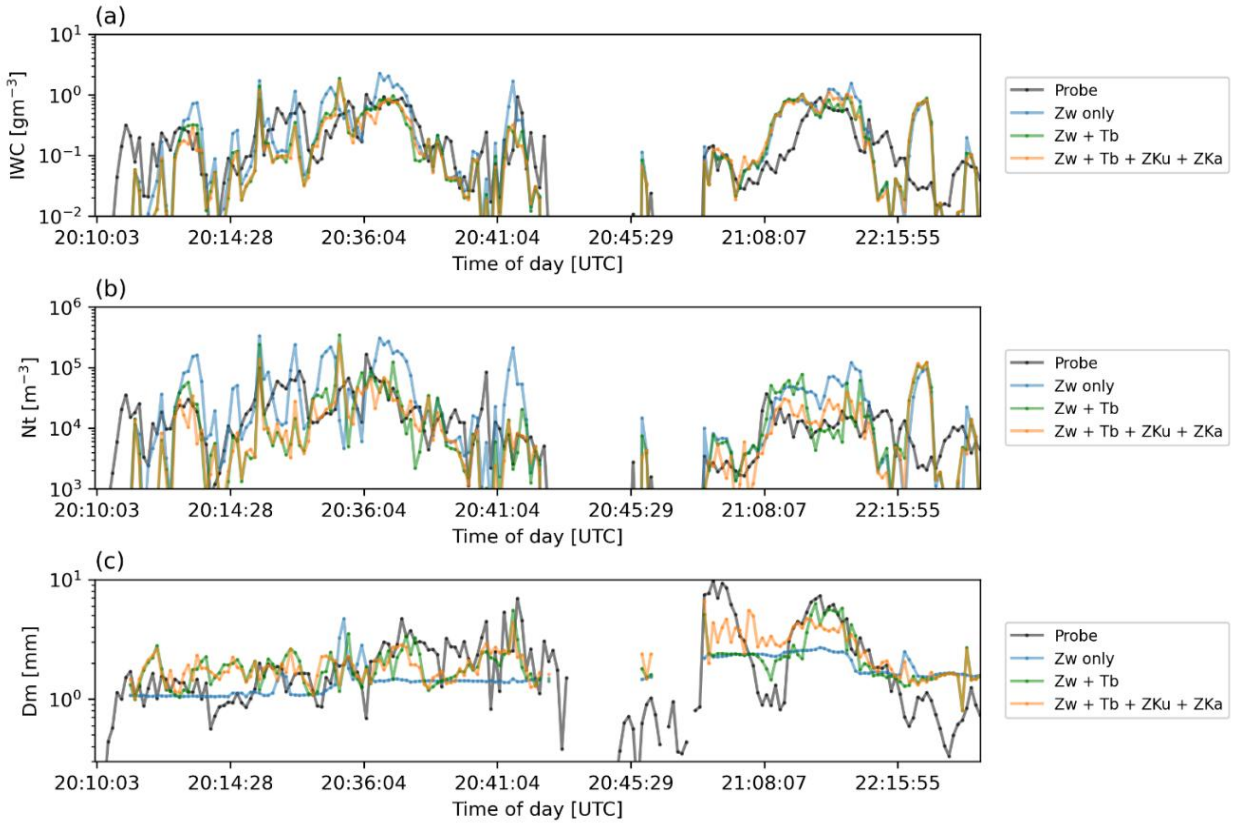

Figure 12: Comparison of (a) IWC, (b) N_t, and (c) D_m between the probe measurements (black lines), Z_w-only retrieved values (blue lines), $Z_w + T_b$ combined retrieved values (green lines), and $Z_w + T_b + Z_{Ku} + Z_{Ka}$ combined retrieved values (orange lines) for the land case on 25 January 2020.

Where does the combined use of multiple sensors most effectively improve the retrieval accuracy? The sensitivity experiment shown in Fig. 5 suggests that the synergistic effect is particularly efficient for large IWCs and small N_ts, or resultingly large particle sizes. In the deeper cloud layers, water deposition and riming tend to increase IWC, while aggregation decreases N_t and increases D_m. Therefore, multi-sensor synergy is expected to enhance retrieval accuracy in deep ice-cloud layers.

Figure 13 shows the improvement in retrieval accuracy by the combined use of multiple sensors relative to the radar-only case as a function of the ice layer depth from the cloud top. The vertical axis represents the reduction in the retrieval error (on a logarithmic scale) against the in-situ probe observations when CoSMIR (T_b) or HIWRAP (Z_{Ku} and Z_{Ka}) measurements are incorporated. ~~The horizontal axis shows IWP$_{above}$~~Positive values indicate an improvement in retrieval accuracy due to the combined use of sensors, whereas negative values indicate a degradation in accuracy. The horizontal axis shows IWP$_{above}$, a proxy for the depth of the cloud layer, defined as the vertically integrated IWC between the cloud top and the flight altitude of

the probe measurement. Despite a considerable scatter, the mean values of bias reduction shown in solid lines indicate that the combined use of multiple sensors improves the retrieval accuracy of N_t and D_m, particularly within the deeper cloud layers (large IWP_{above}). This result supports the improved retrieval accuracy brought by additional instruments as exemplified in Fig. 12. The accuracy improvement with $Z_w + T_b + Z_{Ku} + Z_{Ka}$ is comparable to that with $Z_w + T_b$. ~~As discussed in Fig. 5, this is likely because the high frequency T_b largely provide information independent from Z_w, whereas Z_{Ku} and Z_{Ka} add little new information and have inherently lower sensitivity to ice phase particles~~This may indicate that, as discussed in Fig. 5, high-frequency T_b contains substantial scattering information independent of Z_w. Alternatively, it may simply reflect the limited sensitivity of Z_{Ku} and Z_{Ka} to ice microphysics for the midlatitude snowstorm cases in the IMPACTS campaign and for the altitude range sampled by the in-situ observations. The addition of Ku- and Ka-band radar observations is expected to provide greater benefit for cloud systems such as tropical deep convection that contain larger ice hydrometeors (e.g., hail and graupel). Future work will further investigate the synergy of multi-sensor observations by applying the algorithm to global satellite coincidence datasets.

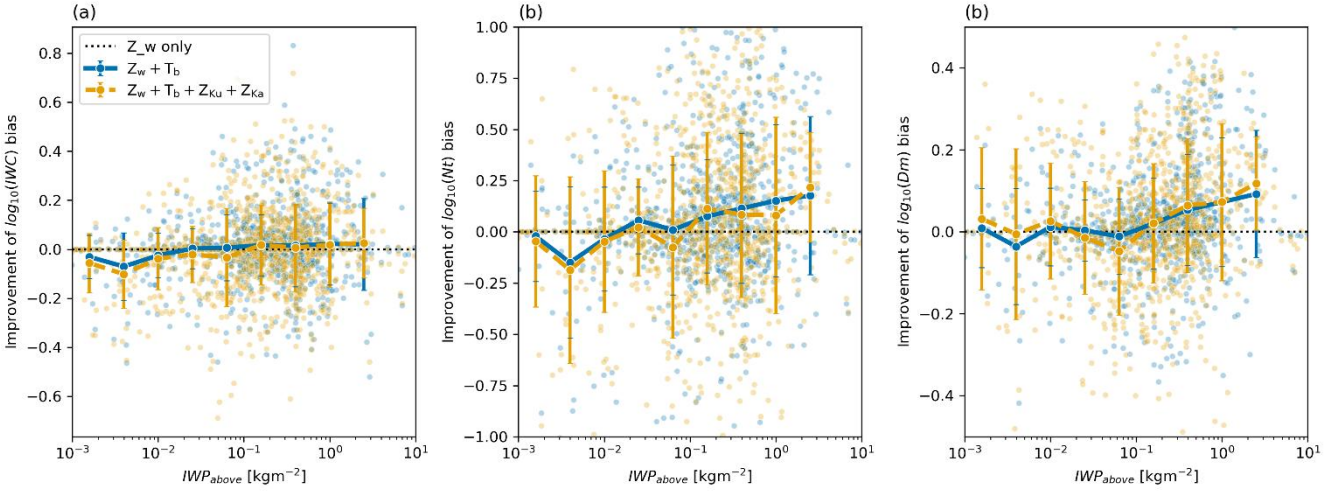

Figure 13: Relationship between the retrieval improvements achieved by combined use of multiple sensors and the depth from the cloud top (IWP_{above}). The black dashed line denotes the baseline accuracy obtained using Z_w only. The light-blue points show the bias reduction obtained from the combined use of Z_w and T_b, while the blue solid line indicates the mean and standard deviation of the bias reduction within each IWP_{above} bin. The orange scatter points and orange dashed line show the corresponding results for the combined use of Z_w, T_b, Z_{Ku}, and Z_{Ka}.

6 Summary

This study evaluates an ice-hydrometer retrieval algorithm which synergistically uses observations from a W-band radar, high-frequency microwave radiometers, Ku- and Ka-band radars. The validation dataset is obtained from the IMPACTS campaign including observations from ER-2 high-altitude aircraft and the P-3 cloud-sampling aircraft. The ER-2 aircraft provides simultaneous measurements from the microwave radiometer (CoSMIR), W-, Ku- and Ka-band doppler radar (CRS and HIWRAP) as inputs to the algorithm (Table 2 and Fig. 2). The P-3 aircraft provides in situ probe measurements of cloud microphysical properties (Table 3 and Fig. 3).

The combined algorithm originally developed in O25 consists of two main components. The first step estimates the initial guess of ice hydrometeor profiles using a training database, and the second step refines these profiles to be consistent with all microwave observations through the optimal estimation method (Fig. 4). The major updates from O25 algorithm are as follows: (1) the incorporation of mixed rosette-snowflake habit with its mixing ratio depending on temperature ; (2) the initial-value estimation scheme has been simplified and generalized; (3) the algorithm has been extended to incorporate Z_{Ku} and Z_{Ka} profiles in addition to Z_w profile and high-frequency T_b; and (4) the estimation of the Z_w-weighted terminal fall velocity (V_t) and the vertical air motion (W).

The retrieved vertical profiles of IWC, N_t, D_m, and V_t are compared with probe measurements (Figs. 6, 7, and 11). Comparisons for all available IMPACTS cases (Table 1) show that all the retrieved microphysical parameters (IWC, N_t, D_m, and V_t) agree well with those from the probe measurements within random noise (Fig. 8). The mean ratios of the retrieved values to ~~prove~~probe measurements for IWC, N_t, and D_m are 1.01, 0.97, and 1.05. The mean bias and RMSE for V_t are −0.02 m s^{-1} and 0.30 m s^{-1} (Fig. 11). These results are obtained under the assumption of the mixed rosette–snowflake particle. Among the 13 particle-habit assumptions tested in this study (Table 4), this mixed habit provides the best overall retrieval accuracy (Fig. 9). Nevertheless, further investigation is required to examine whether this habit assumption is also optimal for other regions, seasons, and cloud types beyond the IMPACTS campaign.

The simulated Z_w, T_b, Z_{Ku}, and Z_{Ka} with the forward model using the retrieved ice-hydrometeor profiles as input closely reproduce the actual ER-2 airborne sensors observations (Fig. 10). This agreement confirms that the current algorithm can retrieve ice-hydrometeor profiles that are consistent with multiple microwave measurements across a wide frequency range.

Sensitivity experiments demonstrate that a synergistic effect obtained from combining multi-sensor observations can be expected where IWC is large and N_t is small—that is, where the particle size is large—owing to the difference in scattering properties between Mie and Rayleigh scattering (Fig. 5). Consistent with this theoretical expectation, the retrieval uncertainties in N_t and D_m, which cannot be sufficiently constrained by Z_w only, are reduced by incorporating high-frequency T_b, Z_{Ku}, and

Z_{Ka} deep inside a cloud layer (Figs. 12 and 13). This result indicates that the combining radars and mm-wave radiometer observations is effective for improving our understanding of the microphysical properties in the deep precipitating clouds beyond the reach of conventional combined radar–lidar measurements.

In the future, this algorithm will be applied to the CloudSat–GPM (Turk et al., 2021) and EarthCARE–GPM (Aoki et al., 2025) satellite matchup datasets to generate a global-scale, long-term dataset of detailed microphysical properties of ice hydrometeors within precipitating systems. The cloud radar onboard the EarthCARE satellite is equipped with the world's first spaceborne Doppler observation capability. The global dataset of the particle fall velocities and the vertical air motion obtained from the Doppler measurements is expected to further advance our understanding of the formation and growth mechanisms of cloud and precipitation particles.

Supplement

The supplement to this article is provided as a separate file.

Code availability

Available upon request.

Data availability

The IMPACTS dataset is available from https://www.earthdata.nasa.gov/data/projects/impacts/collection.

The ER-5 hourly dataset is available from https://cds.climate.copernicus.eu/datasets/reanalysis-era5-pressure-levels?tab=overview.

The forward model used in this study (Joint Simulator for Satellite Sensors) is available from https://www.eorc.jaxa.jp/theme/Joint-Simulator/userform/js_userform.html.

Author contribution

All coding, analysis, and writing of the first draft of this study were performed by KO. The study design, discussions on results, and manuscript improvement were greatly assisted by HM.

Competing interests

The authors declare that they have no conflict of interest.

Acknowledgements

Prof. Guosheng Liu and Assoc. prof. T. Hashino are gratefully acknowledged for making the non-spherical scattering database publicly available and helping us use it in the forward model (Joint Simulator for Satellite Sensors).

This work was supported by the Japan Society for the Promotion of Science (JSPS) KAKENHI under grant no. JP25K07407.

References

Aoki, S., Kubota, T., and Turk, F. J.: Exploring vertical motions in convective and stratiform precipitation using spaceborne radar observations: Insights from EarthCARE and GPM coincidence dataset, EGUsphere [preprint], https://doi.org/10.5194/egusphere-2025-3596, 2025.

Austin, R. T., Heymsfield, A. J., and Stephens, G. L.: Retrieval of ice cloud microphysical parameters using the CloudSat millimeter-wave radar and temperature, J. Geophys. Res., 114, https://doi.org/10.1029/2008jd010049, 2009.

Bailey, M. and Hallett, J.: Growth rates and habits of ice crystals between −20° and −70°C, J. Atmos. Sci., 61, 514–544, 2004.

Bailey, M. P. and Hallett, J.: A Comprehensive Habit Diagram for Atmospheric Ice Crystals: Confirmation from the Laboratory, AIRS II, and Other Field Studies, J. Atmos. Sci., 66, 2888–2899, 2009.

Cazenave, Q., Ceccaldi, M., Delanoë, J., Pelon, J., Groß, S., and Heymsfield, A.: Evolution of DARDAR-CLOUD ice cloud retrievals: new parameters and impacts on the retrieved microphysical properties, Atmos. Meas. Tech., 12, 2819–2835, 2019.

Copernicus Climate Change Service: ERA5 hourly data on pressure levels from 1940 to present, https://doi.org/10.24381/CDS.BD0915C6, 2018.

Delanoë, J., and R. J. Hogan: A variational scheme for retrieving ice cloud properties from combined radar, lidar, and infrared radiometer, J. Geophys. Res., 113, https://doi.org/10.1029/2007JD009000, 2008.

Delanoë, J., and R. J. Hogan: Combined CloudSat-CALIPSO-MODIS retrievals of the properties of ice clouds, J. Geophys. Res, 115, https://doi.org/10.1029/2009JD012346, 2010.

Deng, M., Mace, G. G., Wang, Z., and Paul Lawson, R.: Evaluation of Several A-Train Ice Cloud Retrieval Products with In Situ Measurements Collected during the SPARTICUS Campaign, J. Appl. Meteorol. Climatol., 52, 1014–1030, 2013.

Deng, M., Mace, G. G., Wang, Z., and Berry, E.: CloudSat 2C-ICE product update with a new Z_e parameterization in lidar-only region, J. Geophys. Res., 120, https://doi.org/10.1002/2015jd023600, 2015.

Deng, M., G. G. Mace, Z. Wang, and H. Okamoto: Tropical Composition, Cloud and Climate Coupling Experiment validation for cirrus cloud profiling retrieval using CloudSat radar and CALIPSO lidar, J. Geophys. Res, 115, https://doi.org/10.1029/2009JD013104, 2010.

Draine, B. T. and Flatau, P. J.: Discrete-dipole approximation for scattering calculations, J. Opt. Soc. Am. A Opt. Image Sci. Vis., 11, 1491, 1994.

Eriksson, P., Ekelund, R., Mendrok, J., Brath, M., Lemke, O., and Buehler, S. A.: A general database of hydrometeor single scattering properties at microwave and sub-millimetre wavelengths, Earth System Science Data, 10, 1301–1326, 2018.

Field, P. R., Heymsfield, A. J., and Bansemer, A.: Shattering and particle interarrival times measured by Optical array probes in ice clouds, J. Atmos. Ocean. Technol., 23, 1357–1371, 2006.

Hashino, T., Satoh, M., Hagihara, Y., Kubota, T., Matsui, T., Nasuno, T., and Okamoto, H.: Evaluating cloud microphysics from NICAM against CloudSat and CALIPSO, J. Geophys. Res., 118, 7273–7292, 2013.

Hashino, T., Satoh, M., Hagihara, Y., Kato, S., Kubota, T., Matsui, T., Nasuno, T., Okamoto, H., and Sekiguchi, M.: Evaluating Arctic cloud radiative effects simulated by NICAM with A-train, J. Geophys. Res., 121, 7041–7063, 2016.

Heymsfield, A. J., Schmitt, C, and Bansemer. A.: Ice cloud particle size distributions and pressure-dependent terminal velocities from in situ observations at temperatures from 0 to −86°C, J. Atmos. Sci., 70, 4123–4154, 2013.

Heymsfield, A. J. and Westbrook, C. D.: Advances in the estimation of ice particle fall speeds using laboratory and field measurements, J. Atmos. Sci., 67, 2469–2482, 2010.

Houze, R. A., Jr: Cloud Dynamics, 2nd ed., Academic Press, 2014.

Illingworth, A. J., Barker, H. W., Beljaars, A., Ceccaldi, M., Chepfer, H., Clerbaux, N., Cole, J., Delanoë, J., Domenech, C., Donovan, D. P., Fukuda, S., Hirakata, M., Hogan, R. J., Huenerbein, A., Kollias, P., Kubota, T., Nakajima, T., Nakajima, T. Y., Nishizawa, T., Ohno, Y., Okamoto, H., Oki, R., Sato, K., Satoh, M., Shephard, M. W., Velázquez-Blázquez, A., Wandinger, U., Wehr, T., and van Zadelhoff, G.-J.: The EarthCARE satellite: The next step forward in global measurements of clouds, aerosols, precipitation, and radiation, Bull. Am. Meteorol. Soc., 96, 1311–1332, 2015.

Lawson, R. P., O'Connor, D., Zmarzly, P., Weaver, K., Baker, B., Mo, Q., and Jonsson, H.: The 2D-S (stereo) probe: Design and preliminary tests of a new airborne, high-speed, high-resolution particle imaging probe, J. Atmos. Ocean. Technol., 23, 1462–1477, 2006.

Lawson, R. P., Woods, S., Jensen, E., Erfani, E., Gurganus, C., Gallagher, M., Connolly, P., Whiteway, J., Baran, A. J., May, P., Heymsfield, A., Schmitt, C. G., McFarquhar, G., Um, J., Protat, A., Bailey, M., Lance, S., Muehlbauer, A., Stith, J., Korolev, A., Toon, O. B., and Krämer, M.: A review of ice particle shapes in cirrus formed in situ and in anvils, J. Geophys. Res., 124, 10049–10090, 2019.

Li, L., Heymsfield, G. M., Racette, P. E., Tian, L., and Zenker, E.: A 94-GHz cloud radar system on a NASA high-altitude ER-2 aircraft, J. Atmos. Ocean. Technol., 21, 1378–1388, 2004.

Li, L., Heymsfield, G., Carswell, J., Schaubert, D. H., McLinden, M. L., Creticos, J., Perrine, M., Coon, M., Cervantes, J. I., Vega, M., Guimond, S., Tian, L., and Emory, A.: The NASA high-altitude imaging wind and rain airborne profiler, IEEE Trans. Geosci. Remote Sens., 54, 298–310, 2016.

Liu, G.: A Database of Microwave Single-Scattering Properties for Nonspherical Ice Particles, Bull. Am. Meteorol. Soc., 89, 1563–1570, 2008.

Marshall, J. S. and Palmer, W. M. K.: The distribution of raindrops with size, J. Meteorol., 5, 165–166, 1948.

Mason, S. L., Hogan, R. J., Bozzo, A., and Pounder, N. L.: A unified synergistic retrieval of clouds, aerosols, and precipitation from EarthCARE: the ACM-CAP product, Atmos. Meas. Tech., 16, 3459–3486, 2023.

Masunaga, H.: Satellite Measurements of Clouds and Precipitation, Springer Nature Singapore, 17 pp., 2022.

Masunaga, H., Matsui, T., Tao, W.-K., Hou, A. Y., Kummerow, C. D., Nakajima, T., Bauer, P., Olson, W. S., Sekiguchi, M., and Nakajima, T. Y.: Satellite Data Simulator Unit: A Multisensor, Multispectral Satellite Simulator Package, Bull. Am. Meteorol. Soc., 91, 1625–1632, 2010.

McMurdie, L. A., Heymsfield, G. M., Yorks, J. E., Braun, S. A., Skofronick-Jackson, G., Rauber, R. M., Yuter, S., Colle, B., McFarquhar, G. M., Poellot, M., Novak, D. R., Lang, T. J., Kroodsma, R., McLinden, M., Oue, M., Kollias, P., Kumjian, M. R., Greybush, S. J., Heymsfield, A. J., Finlon, J. A., McDonald, V. L., and Nicholls, S.: Chasing Snowstorms: The Investigation of Microphysics and Precipitation for Atlantic Coast-Threatening Snowstorms (IMPACTS) Campaign, Bulletin of the American Meteorological Society, 103, E1243–E1269, 2022.

Ohara, K., Kubota, T., Kachi, M., and Kazumori, M.: Comparison of long-term total precipitable water products by the Advanced Microwave Scanning Radiometer 2 (AMSR2), J. Meteor. Soc. Japan, 101, 289– 308, doi:10.2151/jmsj.2023-018.

Ohara, K. and Masunaga, H.: Synergy of millimeter-wave radar and radiometer measurements for retrieving frozen hydrometeors in deep convective systems, Atmos. Meas. Tech., 18, 4791–4807, 2025.

Okamoto, H.: Information content of the 95-GHz cloud radar signals: Theoretical assessment of effects of nonsphericity and error evaluation of the discrete dipole approximation, J. Geophys. Res., 107, https://doi.org/10.1029/2001jd001386, 2002.

Okamoto, H.: An algorithm for retrieval of cloud microphysics using 95-GHz cloud radar and lidar, J. Geophys. Res., 108, https://doi.org/10.1029/2001jd001225, 2003.

Okamoto, H., Sato, K., and Hagihara, Y.: Global analysis of ice microphysics from CloudSat and CALIPSO: Incorporation of specular reflection in lidar signals, J. Geophys. Res., 115, https://doi.org/10.1029/2009JD013383, 2010.

Pfreundschuh, S., Eriksson, P., Buehler, S. A., Brath, M., Duncan, D., Larsson, R., and Ekelund, R.: Synergistic radar and radiometer retrievals of ice hydrometeors, Atmos. Meas. Tech., 13, 4219–4245, https://doi.org/10.5194/amt-13-4219-2020, 2020.

Rodgers, C. D.: Inverse Methods For Atmospheric Sounding: Theory And Practice, World Scientific, 256 pp., 2000.

Sato, K., Okamoto, H., Nishizawa, T., Jin, Y., Nakajima, T. Y., Wang, M., Satoh, M., Roh, W., Ishimoto, H., and Kudo, R.: JAXA Level 2 cloud and precipitation microphysics retrievals based on EarthCARE radar, lidar, and imager: the CPR_CLP, AC_CLP, and ACM_CLP products, Atmos. Meas. Tech., 18, 1325–1338, 2025.

Turk, F. J., Ringerud, S. E., Camplani, A., Casella, D., Chase, R. J., Ebtehaj, A., Gong, J., Kulie, M., Liu, G., Milani, L., Panegrossi, G., Padullés, R., Rysman, J.-F., Sanò, P., Vahedizade, S., and Wood, N. B.: Applications of a CloudSat-TRMM and CloudSat-GPM Satellite Coincidence Dataset, Remote Sensing, 13, 2264, 2021.

Wang, J. R., Skofronick-Jackson, G. M., Schwaller, M. R., Johnson, C. M., Monosmith, W. B., and Zhang, Z.: Observations of storm signatures by the recently modified conical scanning millimeter-wave imaging radiometer, IEEE Trans. Geosci. Remote Sens., 51, 411–424, 2013.

Weng, F., Yan, B., and Grody, N. C.: A microwave land emissivity model, J. Geophys. Res., 106(D17), 20115–20123, https://doi.org/10.1029/2001JD900019, 2001.

Wehr, T., Kubota, T., Tzeremes, G., Wallace, K., Nakatsuka, H., Ohno, Y., Koopman, R., Rusli, S., Kikuchi, M., Eisinger, M., Tanaka, T., Taga, M., Deghaye, P., Tomita, E., and Bernaerts, D.: The EarthCARE mission – science and system overview, Atmos. Meas. Tech., 16, 3581–3608, 2023.